Tau aggregation results in an impaired ability to counteract microtubule destabilization via specific combinatorial tau phosphorylation patterns

Nima N Naseri[1,2], Tian Xu[3], Ibrahim Saleh[1], Sapanna Chantarawong[2], Steven M Patrie[3], Neil L Kelleher[3], Manu Sharma[4], Hong Xu[5], Edward B. Lee[5], Ophir Shalem[2,6], Elizabeth Rhoades[1,7]

[1]Department of Chemistry, University of Pennsylvania, Philadelphia, PA, USA

[2]Center for Cellular and Molecular Therapeutics, Children's Hospital of Philadelphia, Philadelphia, PA, USA

[3]Department of Chemistry, Northwestern University, Evanston, Illinois 60208, United States

[4]Appel Institute for Alzheimer's Research, and Feil Family Brain & Mind Research Institute, Weill Cornell Medicine, New York, NY, USA

[5]Department of Pathology and Laboratory Medicine, Perelman School of Medicine at University of Pennsylvania, Philadelphia, PA, USA

[6]Department of Genetics, Perelman School of Medicine, University of Pennsylvania, Philadelphia, PA, USA

[7]Department of Biochemistry and Biophysics, Perelman School of Medicine, University of Pennsylvania, Philadelphia, PA, USA

ABSTRACT

Tau phosphorylation is a defining feature of Alzheimer's disease, yet it also plays an important physiological role in regulating functional interactions with microtubules (MTs), particularly during normal neuronal development. While individual tau phosphorylation sites have been well-studied, how combinatorial phosphorylation impacts tau's behavior in both contexts is poorly understood. We hypothesized that contrasting developmental and pathological models of tau phosphorylation would yield insights into mechanisms of impaired neuronal resilience in tauopathies. We use transgenic PS19 tau mice to demonstrate that increases in individual tau phospho-epitopes with aging do not correlate with their enrichment in tau aggregates in these mice. Using seeded aggregation of tau in neurons, we observe that tau aggregate formation does not necessarily result in MT destabilization; instead, aggregation diminishes tau's ability to counteract destabilization when MTs are externally perturbed. We identify that combinations of tau phospho-signatures are responsive to MT destabilization, and phosphorylation at residues S235 and S262 as particularly critical for regulation of interactions with MTs. Phosphorylation of these residues was associated both with significantly reduced binding to MTs, as well as impaired phosphatase response in aggregates. As a whole, this work provides mechanistic insight into phospho-regulation of tau function and prompts reconsideration of the canonical view that tau phosphorylation precedes MT destabilization in disease. Rather, we provide compelling evidence that phosphorylation of tau may be a response to changes in MT stability and that cell death may result from aggregated tau's inability to function in this manner.

INTRODUCTION

Hyper-phosphorylation of the microtubule (MT)-associated protein tau is strongly correlated with neuropathology in tauopathies including Alzheimer's disease (AD)[1-3]. Substantial evidence supports that tau's properties are significantly altered by post-translational modifications (PTMs) at specific residues, and that accumulation of these phosphate groups is found in intracellular deposits of aggregated tau. There is considerable discrepancy over whether any of these phospho-sites, of which there are over 80 potential sites in tau, are truly causative for aggregation[4] or merely correlated with disease progression. However, several sites are canonically associated with fibrillar aggregates found in disease. These include phosphorylation at sites primarily throughout the proline-rich region (PRR; comprised of domains P1 and P2) and the C-terminal domain at residues T181, S202, T205, T212, S214, T217, T231, S235, S262, S396, S404, S416 and S422 (**Fig. 1A**). Phosphorylation at sites T181 and T217 are currently the most precise tau biomarkers for AD diagnosis[5-8].

The relationship between tau phosphorylation and its physiological state is complex. In numerous organisms, including humans and rodents, tau is highly phosphorylated during normal fetal brain development, underscoring a functional, regulatory role for many phosphorylation sites[9-12]. In fact, many of the same phospho-sites that are canonically associated with tau aggregates in disease are also present at this stage of development, when phospho-tau (p-tau) is highly soluble and functional. Adding to the complexity is that there

are 6 tau isoforms expressed in the adult CNS. The shortest tau isoform, 0N3R (**Fig. 1A**), is exclusively expressed in fetal tissue, whereas isoforms 0N3R, 0N4R, 1N3R and 1N4R comprise the majority of tau in adult brains[13]. However, much of the biochemical tau research has focused on the longest isoform, 2N4R, despite its relatively low fraction in adult brains and negligible presence in fetal brains. The extent to which phospho-regulation of tau function is isoform-dependent is underexplored, but may be particularly relevant in the fetal brain, as the alternatively spliced regions are highly charged (net negative for N-terminal inserts, N; net positive for the repeat-regions insert, R), and thus their inclusion/exclusion may be integral to the effects of negative charges or other physico-chemical changes conferred by phosphorylation.

While the MT-binding domain (MBD) of tau has been the focus of intense research in promoting tau aggregate assembly, the adjacent flanking PRR and R' domains are the primary regulatory regions of tau-MT dynamics. The PRR is the most abundantly phosphorylated domain in tau[14]. Compared to the MBD, the PRR is more competent in promoting MT assembly from soluble tubulin[15], and tau binding to both soluble tubulin and MTs is greatly diminished by phospho-mimic mutations to the PRR[16,17]. The presence of the PRR is critical for tau's ability to bind to MTs[18]; in fact, the MBD shows only weak affinity for MTs on its own[15,19]. Therefore, charge alterations to the PRR by phosphorylation are highly regulatory to tau-MT interactions, likely in a site-specific manner[20-22].

Broadly, phosphorylation to tau is thought to enhance its dissociation from MTs, or inhibit its binding to growing MTs, to facilitate axonal outgrowth during development. Elevated levels of tau phosphorylation have been observed in fetal human brains[11,12], supporting its physiological role in early neurodevelopment. Experimental strategies to increase tau phosphorylation – such as *in vitro* incubation of recombinant tau with kinases[23] or phosphatase inhibition via okadaic acid treatment[24] – can also induce high levels of tau phosphorylation in non-neuronal cell culture models. However, these methods are generally non-specific to phospho-epitopes in tau and may affect multiple substrates beyond tau. The complexity of tau phosphorylation is underscored by its regulation through both physiological and pathological processes. For instance, phosphorylation at one site may prime or enhance phosphorylation at additional sites, illustrating the coordinated action of multiple PTMs to a single tau molecule[25-28]. In disease contexts, phosphorylation at specific residues, such as S262 and S356, has been reported to exert opposing effects on tau's assembly into aggregates[29-32]. Such conflicting findings may reflect the influence of combinatorial PTMs rather than the effects of individual phosphorylation events in isolation.

Furthermore, the mechanisms of compromised neuronal resilience downstream of tau aggregation remain incompletely understood. A prevailing hypothesis is that increased tau phosphorylation and its aggregation reduce tau-MT binding and thus result in destabilized MTs, thereby impairing neuronal health. This view is primarily based upon post-mortem studies reporting overall reductions in MT stability in AD brains[33]. However, closer scrutiny shows no detectable difference in MT stability between neurons containing paired helical filaments and those without[34]. Consistent with this finding, tau knockdown does not destabilize MTs in neuronal cultures; instead, tau appears to associate preferentially with the labile, rather than stable, MT fraction, potentially as a protective mechanism to buffer the MT network against stress[35,36].

Here, we propose to revise the cascade of events in tau pathology by providing a mechanistic link between tau aggregation and alterations to MT stability in neurons. We show that fluctuations in MT growth cycles reshape tau's phosphorylation landscape into specific combinatorial patterns that are canonically associated with insoluble tau. Contrary to longstanding assumptions, in our model system, tau aggregation does not result in destabilized MTs but instead disrupts the neuron's ability to counteract MT destabilization. This loss-of-function is associated with specific phospho-epitopes, especially at S235 and S262, two modifications which significantly disrupt tau from binding to and stabilizing MTs. Our results point to the existence of distinct pools of tau defined by their combinatorial phospho-patterns. Overall, our findings suggest that combinatorial phosphorylation is not only a mechanism for regulating tau function in healthy neurons, but also a potential driver of tau's loss-of-function in disease.

RESULTS

Throughout this study, we used validated antibodies against specific p-tau sites[37-39]. We also validated these antibodies in mouse brains and human iNeurons by tau knockout and knockdown, respectively.

Increases in single phospho-tau epitopes do not correlate with tau aggregation in mouse brains.

Although phosphorylation states have been extensively characterized in tau aggregates, far less is known about how functional phosphorylation patterns are regulated in the developing brain. To begin addressing this gap, we first asked whether individual phosphorylation sites differ between developmental and disease states.

We began by verifying the presence of physiologically phosphorylated tau in fetal mouse brains, in confirmation of prior literature[10-12]. P-tau was readily detected as early as 12 days post-gestation (embryonic day 12, or *E12*) in wildtype embryos, with robust immunoreactivity at several canonical AD-relevant p-tau epitopes, including: S202/T205, T231, S235, S262, S396, S404, S416 and S422 (**Fig. 1B**). Tau phosphorylated at S404 was also detected in embryonic primary neuron cultures (**Fig. 1C**). Notably, the localization patterns for pS404 and α-tubulin were extremely similar, suggesting that tau that is phosphorylated at S404 remains capable of associating with MTs.

Because tauopathies such as AD are characterized by an aberrant, age-related increase in p-tau, we next compared tau phosphorylation patterns between neonatal mouse brains – representing a developmental stage with physiologically high levels of tau phosphorylation – and aged PS19 tauopathy mouse brains – a time when tau phosphorylation is largely ectopic. The PS19 tauopathy mouse model overexpresses the 1N4R isoform of tau harboring the pathogenic P301S mutation and develops insoluble tau deposits by 3 months of age[40]. We examined p-tau forms in neonatal (P0) and 9-month-old PS19 mouse brains by fractionating soluble and insoluble proteins and probing them using a panel of 11 site-specific p-tau antibodies (**Fig. 1D**).

Although most tau remained soluble at both times points (97.6% at P0; 89.7% at 9-months), the overall abundance of insoluble tau, as quantified by pan-tau (Tau5), was approximately 4-fold more in the 9-month-old

compared to neonatal PS19 mouse brains (**Fig. 1D,E**). Numerous p-tau epitopes were detectable in aged PS19 mice, and a clear mass shift distinguished neonatal 0N3R tau from 1N4R tau at 9-months. The extent of phosphorylation was quantified by normalization to pan-tau to reveal heterogeneity across phospho-epitopes at 9-months relative to P0. To illustrate, phosphorylation at sites T212/S214 (AT100 epitope) and S235 increased markedly with age (>3-fold and >4-fold increase, respectively); in contrast, phosphorylation levels were a fraction of those found in neonates at sites S202/T205 (~93% lower), T231 (~72% lower), S262 (~64% lower) and S396 (~70% lower). No significant differences were observed between P0 and 9-months at sites T181, T217, S404, S416 or S422, suggesting comparable phosphate occupancy at these sites across both timepoints. Together, these results highlight conserved and divergent patterns of tau phosphorylation that may distinguish physiological from pathological modifications.

Next, we sought to investigate whether p-tau was preferentially enriched in insoluble tau, by comparing soluble p-tau against soluble total tau (**Fig. 1D,F**). In this quantification, we expected that in the absence of preferential enrichment, the fraction of p-tau found in the soluble fraction would be very similar to the total fraction of soluble tau protein. For the neonatal brains, we observed almost exactly this, with the fraction of soluble p-tau indistinguishable from soluble total tau across epitopes. However, at 9 months, we found several phospho-epitopes were more abundant in the insoluble fraction, especially at S202/T205 (~61% soluble), T212/S214 (~33% soluble), T217 (~50% soluble) and strikingly at S422 (~17% soluble). Additional phospho-sites such as T181 (~82% soluble), T231 (~75% soluble), S235 (~84% soluble) and S262 (~75% soluble) showed moderate enrichment in the insoluble fraction with age. In contrast, phosphorylation at C-terminal sites S396 (~94% soluble), S404 (~91% soluble) and S416 (~94% soluble) largely reflected the fraction of soluble tau. In the 9-month-old mice, insoluble p-tau species were frequently mass-shifted upwards compared to soluble p-tau, consistent with more heavily modified insoluble tau species.

Collectively, these data indicate that although neonatal and tauopathy aged brains share many phospho-epitopes, fetal p-tau is generally not found in aggregates. This divergence between physiological phosphorylation in the fetal brain and ectopic phosphorylation during aging may give rise to distinct p-tau species, some of which may be unique to either state. However, changes in total p-tau abundance with age did not correlate with enrichment in the insoluble fraction (**Fig. 1G**). To illustrate, phosphorylation increased at T212/S214 by >3-fold and decreased at S202/T205 by >90% with age, yet both epitopes were strongly enriched in the insoluble fraction. These findings indicate that single phospho-epitopes cannot reliably predict tau aggregation, underscoring the need to evaluate combinatorial phosphorylation rather than individual sites in isolation.

Human iNeurons provide a platform for contrasting physiological and pathological p-tau.

The lack of clear, single-epitope distinctions between developmental and pathological tau phosphorylation *in vivo* prompted us to seek a neuronal culture model that would allow us to examine tau phosphorylation not only at individual sites, but also in combination. However, endogenous, non-overexpression

175 models for studying tau phosphorylation have not been widely reported. Extensive phosphorylation to the fetal
176 tau isoform, 0N3R, is reported in multiple organisms including developing avians[9], rodents[10] and humans[11,12],
177 suggesting that a naïve neuronal model may naturally support high levels of physiological p-tau. We therefore
178 turned to human iPSC-derived induced neurons (iNeurons), which recapitulate key features of the embryonic
179 environment[41-43], for our studies.

180 Using iNeurons, we applied top-down mass spectrometry to quantify phosphorylation stoichiometries on
181 intact endogenous tau. High levels of p-tau were readily detected, with a mean of 12.2 and median of 12.0
182 phosphates per tau protein. Phosphorylation levels were quantitatively characterized by four distinct clusters of
183 1-6, 7-10, 11-18, or 19-21 phosphates per tau molecule (**Fig. 2A & S1**). Within each cluster, the mode was 5, 8,
184 14 and 19 phosphates per tau. Acetylation was detected only on tau molecules modified with at least 11
185 phosphates (**Fig. S1**). Based on past qualifiers that >7 phosphates constitute tau hyperphosphorylation[12], these
186 data indicate that ~82% of endogenous fetal tau in iNeurons meet this criterion. Thus, iNeurons express diverse,
187 highly phosphorylated populations of tau molecules that are modified in potentially distinct combinatorial
188 phospho-states.

189 Using a panel of tau phospho-epitope antibodies, as in 'Figure 1', we detected a number of the same AD-
190 relevant phosphorylation modifications to tau in iNeurons as in brain tissue, including at sites T181 (AT270
191 epitope), S202/T205 (AT8 epitope), T212, T217, T231 (AT180 epitope), S235, S262, S396, S404 and S416 (**Fig.
192 S2A**). Despite exclusively using previously validated p-tau antibodies, their specificity has not been confirmed in
193 iNeurons. To address this, we generated a tau knockdown (tau^{KD}) iPSC line using CRISPR-interference.
194 Following neuronal differentiation, tau expression was nearly abolished relative to a non-targeting control (NTC)
195 sgRNA (**Fig. S2B**), and unlike tau knockout models, tau knockdown was not compensated by upregulation of
196 other MT-associated proteins (MAP1A, MAP1B, MAP2) (**Fig. S2C**). A further advantage of this tau^{KD} model is
197 the ability to reintroduce tau by lentiviral transduction at approximately endogenous levels on a clean background
198 (**Fig. S2D**), enabling measurements on individual isoforms without confounding compensation by other MAPs.
199 Importantly, p-tau antibody specificity for tau was clearly demonstrated, apart from epitopes T212/S214, S214
200 (independently) and S422 (**Fig. S2E**).

201 Together, these results establish human iNeurons as a robust, endogenous model of fetal tau
202 phosphorylation. The high stoichiometries of phospho-epitopes underscore the physiological importance of
203 combinatorial phosphorylation during neuronal development and provide a powerful platform for contrasting
204 physiological and pathological p-tau signatures.

205

206 ***Tau aggregation impairs the neuron's ability to counteract MT destabilization.***

207 To investigate how tau aggregation affects tau phosphorylation and MT stability, we next established a
208 tau pathology model in human iNeurons by seeding endogenous tau using either AD brain-derived insoluble tau
209 (**Fig. 2B**) or recombinant 3R tau seeds (**Fig. S3A**). Four to eight weeks after seeding, tau aggregation was

robustly induced with AD brain-derived seeds (**Fig. 2C-ii & S3B-ii**) and less so with recombinant 0N3R seeds (**S3B-iii**), appearing as puncta or elongated structures within the soma and neurites, which were absent from unseeded controls (**Fig. 2C-i & S3B-i**).

Tau aggregation is thought to reduce MT stability by depleting soluble tau that would normally be associated with MTs. Thus, we expected to observe MT destabilization in our pathology model. Instead, we found the opposite: MTs remained largely intact in neurons harboring abundant tau aggregates (**Fig. 2D & S3C**). Following extraction of soluble tubulin, quantification of polymerized tubulin revealed a significant increase in total MT levels following seeding (**Fig. 2D & S3D**). Western blot against K40-acetylated α-tubulin, a marker of stable MTs, further corroborated that MTs remained stable as long as 8 weeks post-seeding (**Fig. 2E & S3E**).

This unexpected observation led us to revisit tau's physiological function. Given some evidence that tau preferentially associates with labile tubulin and protects MTs from destabilizing enzymes[35,36,44], we hypothesized that tau may serve not only to stabilize MTs but to buffer the MT lattice against destabilizing stress. If so, sequestration of tau into aggregates should reduce this protective capacity.

To test this, we challenged the MT network with nocodazole, a small molecule that destabilizes MTs by sequestering soluble tubulin heterodimers. Nocodazole disrupted MTs in all conditions, but the magnitude of MT loss was markedly greater in seeded neurons (**Fig. 2F** & **S3C,F**). Following nocodazole treatment, K40-acetylated α-tubulin decreased by 48% in AD-seeded neurons and 37% in 3R-seeded neurons compared to unseeded controls. As a whole, these data support a model in which tau aggregation renders neurons more vulnerable to MT destabilization, consistent with the loss of tau's endogenous ability to counteract MT stress.

We next asked whether any specific p-tau epitopes could be connected to this phenotype. We quantified changes to site-specific tau phosphorylation levels in DMSO- and nocodazole-treated conditions, with and without seeding (**Fig. 2G & S3G**). In unseeded neurons, MT destabilization by nocodazole resulted in general trends toward dephosphorylation at many epitopes, consistent with MT destabilization triggering tau-targeted phosphatase activity to increase tau binding to soluble tubulin and/or MTs. In seeded neurons, the baseline levels of tau phosphorylation were higher at most epitopes relative to unseeded neurons. Remarkably, the seeded neurons exhibited a similar pattern as the unseeded ones following nocodazole treatment, with p-tau levels reduced to those of unseeded neurons, except at two epitopes, S235 and, most strikingly, S262. At S262, nocodazole induced a ~31.5% reduction in phosphorylation in unseeded neurons but substantially less dephosphorylation in seeded neurons.

These results challenge the canonical tau cascade by demonstrating that increased tau phosphorylation and aggregation are not sufficient to significantly destabilize MTs. Rather, our data supports a model in which tau aggregation disrupts the neuron's ability to buffer the MT network, increasing neuronal susceptibility to MT stress, likely primarily due to unavailability of sufficient amounts of soluble, functional tau. Dephosphorylation to increase MT affinity of tau may also be dysregulated at critical tau phospho-epitopes, especially S262.

245 ***Phospho-sites are co-regulated in specific patterns in response to MT growth cycles.***

246 In general terms, phosphorylation to tau is thought to decrease binding of tau to MTs, facilitating MT
247 depolymerization. In the developmental context, neurons maintain highly dynamic MTs, which undergo cycles of
248 growth and shrinkage; our results here also show that they have high stoichiometries of tau phosphorylation
249 (**Fig. 2A**). However, our seeding experiments suggest that tau phosphorylation levels can also be altered in
250 response to changes in MT stability, not solely preceding MT destabilization.

251 We sought further insight into the response of p-tau changes to MT stability by pharmacologically
252 perturbing the neuronal cytoskeleton and measuring the impact on site-specific tau phosphorylation. MTs were
253 destabilized using either nocodazole or demecolcine or stabilized using paclitaxel; as a control, actin filaments
254 were depolymerized using latrunculin A (**Fig. S4**). For clarity across all experiments, we consolidated phospho-
255 sites responses into four categories based on observed trends by the following color scheme: gray (T181, S396),
256 blue (S202/T205, T212, T217), red (T231, S235, S262) and magenta (S404, S416). We consistently maintained
257 this consolidated grouping (also seen in **Fig. 1A**) throughout the remainder of the analyses. Data corresponding
258 to each independent phospho-epitope are available in the supplementary information.

259 Consistent with our seeding results, MT disruption by demecolcine reproduced the effects of nocodazole
260 by inducing pronounced tau dephosphorylation at numerous phospho-epitopes including S202/T205, T212 and
261 T217, and more modest dephosphorylation at T231, S235 and S262. Intriguingly, MT disruption resulted in
262 increased tau phosphorylation in the C-terminus at epitopes S404 and S416. MT stabilization by paclitaxel
263 produced similar tau dephosphorylation patterns at epitopes S202/T205, T212, T217, though effects at T231,
264 S235 and particularly S262 were less pronounced. In contrast, actin depolymerization had minimal effects on
265 tau phosphorylation at most of the measured epitopes, indicating that these signatures are primarily driven by
266 MT perturbation. Together, these results suggest that tau phosphorylation is differentially regulated in response
267 to changes to MT stability, rather than acting solely as its upstream effector.

268 We further expanded upon this finding to measure how tau phosphorylation is modulated in response to
269 MT collapse and re-stabilization. In this paradigm, acute MT catastrophe was induced in iNeurons using a brief
270 (5 minute) cold exposure followed by either short- or long-term nocodazole treatment for 15 or 90 minutes,
271 respectively, to analyze the cellular response to acute versus sustained MT damage. After 90 minutes,
272 nocodazole was washed out to allow MT recovery (**Fig. S5A**). We tracked site-specific phosphorylation to tau
273 throughout the treatment and recovery periods.

274 As expected, nocodazole disrupted the spindle-like MT lattice and tau's axonal localization, both of which
275 recovered within 3 hours after nocodazole washout (**Fig. S5B**). These visual findings were corroborated by
276 immunoblot against K40-acetylated α-tubulin and detyrosinated α-tubulin, an orthogonal marker of stable MTs,
277 which were reduced to ~50% of control levels and recovered to ~75% at 3 hours after nocodazole washout (**Fig.
278 3A,B**).

279 We then correlated dynamic changes in tau phosphorylation with MT collapse and re-stabilization (**Fig.**

280 **3A,C** and **S5C**). Tau phosphorylation dynamics could be classified into four distinct groups.

281 The first group, comprised of T181 and S396 (gray line), was not significantly impacted by nocodazole
282 treatment or washout. The second group (S202/T205, T212, T217; blue line) consisted of rapid responders,
283 which underwent strong dephosphorylation (~23% of control levels) in response to nocodazole treatment
284 followed by rapid re-phosphorylation after nocodazole washout (recovery to ~64% of control levels). These
285 epitopes closely mirrored the changes to MT stability throughout the time course. The third group (T231, S235
286 and S262; red line) consisted of delayed responders, which exhibited slower and more modest
287 dephosphorylation in response to nocodazole treatment (~45% of control levels), with limited levels of re-
288 phosphorylation after nocodazole washout (recovery to ~54% of control levels). These sites changed more slowly
289 than the blue cluster, and continued to decrease until 1 hour into the recovery phase, even after detyrosinated
290 α-tubulin and acetylated α-tubulin levels had stabilized. The fourth group (S404, S416; magenta line) consisted
291 of inverse responders, which were rapidly phosphorylated within 15 min of MT collapse: phosphorylation at these
292 sites continued to increase until the nocodazole was washed out (~175% of control levels), at which point these
293 sites were immediately, rapidly dephosphorylated (~65% of control levels) in alignment with the timescale of MT
294 stabilization, highlighting an inverse relationship with MT integrity. The prompt increase in phosphorylation at
295 these two epitopes may reflect the importance of regulation at these sites for counteracting MT destabilization.

296 Nocodazole treatment did not impact total (pan) tau or β-tubulin III levels, though both proteins showed
297 modest upregulation after nocodazole washout, suggesting a potential compensatory cellular response to
298 counteract MT destabilization (**Fig. 3A,B**). Notably, changes to tau phosphorylation preceded any detectable
299 increases in protein abundance; therefore, the observed patterns of dephosphorylation and phosphorylation
300 were independent of new protein synthesis.

301 Overall, our data show that tau phosphorylation is dynamically and combinatorially regulated by MT
302 stability. Co-regulated clusters, including T181-S396, S202/T205-T212-T217, T231-S235-S262 and S404-S416,
303 may reflect distinct roles in MT collapse and recovery, supporting a model in which tau phosphorylation
304 signatures act as responders to MT integrity rather than solely as drivers of MT destabilization.

305

306 ***Tau dephosphorylation by PP2a is necessary to counteract MT destabilization.***

307 The co-regulated phosphorylation patterns identified above suggest that p-tau exists in distinct pools that
308 respond differentially to MT stress. As MTs undergo collapse, many of the p-tau sites we probed are
309 dephosphorylated, shifting the equilibrium toward increased tau binding to MTs as a compensatory mechanism
310 to counteract MT catastrophe. As cellular conditions become conducive to MT recovery or repair, these same
311 sites are re-phosphorylated, tipping the balance back toward less MT-bound tau and restoring dynamic flexibility.
312 This regulatory model contrasts with the prevailing view in neurodegeneration that phosphorylation to tau
313 primarily drives MT destabilization by disrupting tau's MT-binding capacity. In contrast, our seeding experiments
314 showed that even large increases in tau phosphorylation, accompanied by sequestration of tau into aggregates,

315 did not result in destabilized MTs (**Fig. 2E**), raising the possibility that changes in MT stability precede and
316 influence site-specific tau phosphorylation. Taken together, these observations suggest that tau phosphorylation
317 can function both as a consequence and a driver of MT stability, with the directionality of this relationship
318 potentially differing between physiological and pathological states.

319 To further investigate, we probed the molecular pathways that regulate tau dephosphorylation and
320 phosphorylation during MT collapse and recovery. We first characterized the activation states of a phosphatase
321 and kinases that have been previously implicated in tau regulation[10,25]. The phosphatase PP2a was activated
322 during nocodazole treatment, coinciding with the period of tau dephosphorylation (**Fig. 4A,B**, *top panels*). The
323 kinases Erk1/2 and Akt1 were activated after nocodazole washout, temporally aligning with the period of tau re-
324 phosphorylation (**Fig. 4A,B**, *middle two panels*), whereas the kinase GSK3β was activated as soon as 15
325 minutes after nocodazole treatment (**Fig. 4A,B** *bottom panels*), preceding the period of phosphorylation of most
326 tau sites except for S404 and S416.

327 We next asked whether inhibiting these enzymes could alter MT stability. We combined phosphatase
328 inhibition with nocodazole treatment to assess the role of tau dephosphorylation during MT collapse, and applied
329 kinase inhibition during the recovery period to test for the impact of blocking tau phosphorylation during MT
330 recovery. Among the kinase inhibitors that we tested – targeting Akt1 (AKT1 inhibitor VIII), Erk1/2 (Erk1/2 inhibitor
331 I) and GSK3β (BIO) – only the Akt1 inhibitor was both effective and selective for its intended target in iNeurons
332 during the tested timeline (**Fig. S6A,B**). Akt1 inhibition resulted in only a modest improvement in MT stability
333 compared to DMSO treatment (**Fig. S6B**). These results suggest that blocking tau phosphorylation at sites that
334 are targeted by Akt1 during MT recovery has a limited effect on MT stabilization. Instead, these findings imply
335 that the critical regulatory response to counteracting MT destabilization may not occur during re-phosphorylation
336 but rather during the dephosphorylation phase, when tau must rapidly respond to MT damage.

337 Accordingly, we inhibited PP2a activity using either LB-100 (reversible) or Calyculin A (potent,
338 irreversible) during nocodazole treatment. Both inhibitors effectively reduced PP2a activity (**Fig. S6C**). LB-100
339 treatment impaired MT stability during nocodazole treatment but MTs were able to recover after washout (**Fig.
340 4C,D & Fig. S6C**). In contrast, Calyculin A treatment led to severe MT destabilization, comparable to AD-seeded
341 conditions (**Fig. 2F**), and MTs failed to recover after washout, consistent with the irreversible nature of inhibition.

342 Finally, we correlated changes in MT stability with epitope-specific changes in tau phosphorylation. Mild
343 PP2a inhibition by LB-100 was compared to potent inhibition by Calyculin A to tease out specific tau phospho-
344 epitopes that may be critical for MT recovery. PP2a inhibition correlated with blunted dephosphorylation at many
345 epitopes (S202/T205, T212, T217, T231, S235 and S262), while sites T181, S396, S404 and S416 remained
346 largely unaffected (**Fig. 4C,E & S7**). Of note, Calyculin A treatment resulted in especially higher levels of
347 phosphorylation at sites T212, S235, and most prominently at S262. While we do not ascribe causal roles to
348 individual epitopes, the disproportionate sensitivity of S235 and S262 to phosphatase inhibition, as well as their
349 delayed re-phosphorylation following nocodazole treatment (**Fig. 3C & S5**), underscores that dephosphorylation
350 of these residues was closely linked to the cell's ability to restore MT stability following collapse.

Together, these findings demonstrate that PP2a activation is required for neurons to buffer against MT destabilization, and that distinct subgroups of tau phospho-sites are tightly linked to this response. This establishes that tau dephosphorylation is not passively correlated with counteracting MT destabilization but is a component of the neuronal response to MT catastrophe.

Tau phosphorylation at T231, S235 and S262 directly and substantially disrupt tau-MT interactions.

Our data demonstrate that fetal tau is modified at many of the same phospho-epitopes as pathology-associated tau, and in some cases to a greater extent, yet tau remains functional and MTs are stable in the developing brain. Given that different p-tau species were observed to be co-regulated in certain clusters in response to chemical destabilization of MTs, we asked whether these same clusters differ in their physical associations with MTs. Tau phosphorylation regulates tau-MT interactions, although molecular details are lacking for many individual phosphorylation sites, and combinatorial effects are even more poorly characterized. Therefore, we fractionated intact MTs from tau^{KD} iNeurons expressing 0N3R tau and compared phospho-site associations with MTs for tau.

Effective MT fractionation was indicated by separation of detyrosinated α-tubulin from neuron-specific enolase (NSE), a marker for neuronal cytosol and plasma membrane (**Fig. 5A & S8**). Approximately 77% of β-tubulin III and 43% of tau was found in the intact MT fraction.

We then quantified the distribution of phospho-sites across both fractions (**Fig. 5A**). Tau phosphorylated at sites in the late P2 domain (T231, S235) and in the R1 domain (S262) was almost exclusively in the cytosol, indicating that phosphorylation at these sites is strongly associated with MT dissociation. In contrast, phosphorylation at more N-terminal P2 domain sites (T181, S202/T205, T212 and T217) and within the C-terminal domain (S396, S404, S416) was more strongly associated with MTs. These localizations are consistent with the idea that the PRR can regulate tau-MT binding independently of the MBD. Overall, we observed a bimodal distribution, in which tau that was phosphorylated outside of the last 15 residues of the P2 domain in the PRR + early MBD residues (T231, S235, S262) was more likely to be associated with the MT fraction compared to those within this region.

We then integrated these observations with our MT growth-cycle experiments to provide insight into the relationship between MT-association and responsiveness of tau to MT integrity (**Fig. 5B**). The cluster of sites that showed the slowest re-phosphorylation after nocodazole washout (T231, S235, S262) also exhibited the lowest levels of MT-binding. This alignment suggests that these sites must remain dephosphorylated for tau to effectively engage MTs during recovery. In contrast, epitopes that showed minimal changes or rapid re-phosphorylation after nocodazole washout (T181, S396, S202/T205, T212 and T217) were comparatively enriched in the MT-bound fraction, consistent with a model in which their phosphorylation state is less restrictive for MT association.

386 The alignment between the clusters of behavior of phospho-sites within these data sets reveals a
387 hierarchy of which sites are most critical for regulating functional interactions of tau with tubulin/MTs. The striking
388 sensitivity of S235 and S262 to both phosphatase inhibition and MT-binding assays reinforces their central
389 position in regulating tau-MT interactions.

390 Thus far, these data demonstrate that tau phosphorylation changes are strongly correlated with its
391 association with MTs and the observed alterations to MT stability in the presence of MT stressors. To directly test
392 for a link between site-specific tau phosphorylation and MT stability, we turned to a cell-free system to model
393 and validate these biophysical interactions.

394 While phospho-mimetic substitutions are widely used, they do not reproduce endogenous combinations
395 of modifications, and their ability to accurately mimic bonafide phosphorylation remains uncertain. To address
396 this, we cloned, expressed and purified wildtype 0N3R tau along with single-site phospho-mimetic substitutions
397 (Thr→Glu or Ser→Glu) at key sites identified from our neuronal dataset: T181, T217, T231, S235, S262, S396
398 and S404. We also generated three combinatorial phospho-mimetics: T231E/S235E and T231E/S262E, as well
399 as S396E/S404E based on its relevance to tau fibrils.

400 Using tubulin purified from bovine brains, we assessed the capacity of each tau variant to promote
401 polymerization of soluble tubulin (**Fig. 5C**). Most single-site phospho-mimetics impaired MT polymerization
402 compared to their wildtype counterparts. Of the individually tested phospho-mimetics, the S235E and S262E
403 mutations of MT polymerization (~46% and ~73% reduction, respectively). Combinatorial phospho-mimetics
404 revealed further that dual glutamate substitutions at T231/S235 and T231/S262 resulted in additive inhibition of
405 MT polymerization activity: In fact, these combinations impaired tau activity more than would be predicted from
406 the individual mutations. Consistent with our observations in neurons, phospho-mimetic mutations at S396E,
407 S404E and in combination had comparatively modest effects on MT polymerization.

408 These experiments reinforce our finding that phosphorylation particularly at S235, S262 and in
409 combination with T231 directly impair tau's ability to bind to tubulin/MTs. In support, correlation of p-tau bound to
410 MTs (from iNeurons) with MT polymerization rates (from recombinant proteins) emphasized a clear disruption by
411 site-specific phosphorylation/phospho-mimics to tau's (R^2=0.480) interaction with MTs (**Fig. 5D**). Our data
412 support prior predictions that S235 and S262 make more contacts with MTs relative to other phospho-epitopes,
413 suggesting that phosphorylation at these residues plays a particularly critical role in modulating MT stability[20].

414

415 ***Tau is phosphorylated in site-specific combinatorial patterns in iNeurons.***

416 Finally, we asked whether the regulation of site-specific tau phosphorylation in iNeurons aligns with
417 patterns of co-phosphorylation. In pursuit, we next asked whether phosphorylation patterns are random or occur
418 in distinct combinations. This question is essential because Western blot-based measurements cannot resolve
419 combinatorial PTMs on individual tau molecules. Meanwhile, our earlier measurements indicate that tau-MT
420 interactions may be dependent upon combinatorial phosphorylation to tau rather than single modifications.

421 Although several dual-phosphorylation events have previously been observed in tau aggregates (e.g.,
422 S202/T205, T212/S214, T231/S235 and S396/S404[45-49]), combinatorial occurrences of tau phosphorylation are
423 generally understudied, in particular as relevant to tau function.

424 We began to quantify these patterns by first immunoprecipitating p-tau from tau^{KD} iNeurons expressing
425 0N3R^{EGFP} and back-calculating phosphorylation frequencies by comparing the recovery of phospho-specific tau
426 with total tau captured in each immunoprecipitation[50]. This allowed us to estimate the proportion of tau molecules
427 phosphorylated at a given epitope. In agreement with the top-down mass spectrometry results, we found
428 abundant and heterogeneous phosphorylation levels: pT217 and pS235 were uncommon (<20%), pT181 and
429 pT212 were moderately common (>20%), and pS202/pT205, pT231 and pS396 were abundant (>45%) (**Fig.
430 S10**).

431 To investigate co-occurrence between phosphorylation sites, we asked: when tau is phosphorylated at a
432 given site, what is the likelihood that it is also phosphorylated at a second site? To address this question, we
433 immunoprecipitated p-tau at individual phospho-epitopes targeting prominent AD-relevant epitopes within the
434 PRR (T181, S202/T205, T212, T217 and T231) and one epitope in the C-terminus (S396), then probed for co-
435 occurring phosphorylation at additional sites (**Fig. 6A,B**). Co-occurrence frequencies were calculated as the
436 signal for each secondary phospho-site (normalized to input) divided by the signal for the primary
437 immunoprecipitated site (also normalized to input).

438 This approach yielded numerous unique patterns of co-occurring phospho-sites, indicating that tau
439 phosphorylation follows non-random, site-specific patterns (**Fig. 6C**). Two previously established combinations,
440 pS396/pS404 and pT231/pS235, were among the most frequently observed combinations, validating our
441 approach. Specifically, phosphorylation at S396 conferred a ~61% likelihood of concurrent phosphorylation at
442 S404. Similarly, tau phosphorylated at T231 exhibited a ~41% likelihood of co-occurring phosphorylation at S235.

443 We next sought to identify novel patterns of tau phosphorylation by ranking the top ten most common
444 pairwise co-occurrences (**Fig. 6D**, *left column*). From highest to lowest co-occurrence, the most prominent dual
445 combinations of phospho-epitopes were as follows (with the immunoprecipitated site <u>underlined</u>):
446 pS202/pT205/<u>pS396</u> (68%); <u>pS396</u>/pS404 (61%); <u>pS202/pT205</u>/pT212 (61%); pT181/<u>pS396</u> (58%);
447 pT212/<u>pT217</u> (54%); pT181/<u>pS202/pT205</u> (52%); pT212/<u>pS396</u> (46%); pT181/<u>pT217</u> (45%); pT181/<u>pT231</u>
448 (42%); <u>pT231</u>/pS235 (41%). Additionally, tau phosphorylated at S262 exhibited 30% linkage with pT212.

449 Asymmetric linkages were also evident. For instance, pT217 was also phosphorylated at T212 in ~54%
450 of cases, but the reverse relationship was not as prevalent: only ~8% of tau phosphorylated at T212 also carried
451 phosphorylation at T217. Such asymmetric patterns may reveal potential priming or hierarchical ordering of tau
452 phosphorylation events.

453 Next, we explored this dataset to infer potential combinations of three simultaneous co-occurrences.
454 Pairwise probabilities cannot infer higher-order combinations; therefore, we applied minimum-linkage analysis
455 to estimate the likelihood of triplet co-occurrences by selecting the weakest link among the triplets. Using this

relatively conservative metric, the top ten most likely sets of three simultaneously co-occurring tau phospho-epitopes were ranked from highest to lowest (**Fig. 6D**, *right column*). Some of the most frequent co-occurrences, such as T231-S262-S396, may represent specific tau phospho-proteoforms (**Fig. 6E**).

The pairwise and triplet analyses revealed robust linkages between specific phospho-epitopes, aligning with the sites that we had earlier grouped into clusters. Frequent co-occurrences were observed between S202/T205, T212 and T217, forming a tightly associated cluster (color-coded blue). A second cluster emerged linking T231 with S235 and S262 (color-coded red). In contrast, phosphorylation at T181 and S396 was broadly distributed, indicating more promiscuous co-occurrence patterns (color-coded gray). Finally, S404 and S416 co-occurred most strongly with S396, and to a lesser extent with T217 and T212, forming a distinct subgroup (color-coded magenta).

These structured patterns suggest that tau phosphorylation is a coordinated process. The frequent co-occurrence of certain phospho-epitopes may reflect coordinated regulation by shared kinases or shared functional consequences in modulating tau's biochemical properties and behavior. Accordingly, specific combinations of phosphorylation may define distinct pools of tau, each potentially associated with unique functional roles.

Importantly, the most prominent phosphorylation co-occurrences mirrored the patterns of dephosphorylation and re-phosphorylation in response to MT depolymerization and recovery (from **Fig. 3C**). For instance, pS202/pT205 and pT212 (~61% co-occurrence), pT212 and pT217 (~54% co-occurrence), pT231 and pS235 (~41% co-occurrence), and pT181 and pS396 (~58% co-occurrence) were similarly impacted by nocodazole treatment and washout. These coordinated changes support the notion that these sites are not only frequently co-phosphorylated but also co-regulated in response to shifts in MT stability. Combined with our functional data, these findings support a model in which combinatorial phosphorylation encodes specific tau proteoforms with functions that are tightly integrated with MT dynamics and cellular resilience.

DISCUSSION

PTMs like phosphorylation diversify the functions of proteins. Tau is a striking example of PTM complexity, with over 80 potential phosphorylation and 40+ potential acetylation sites, as well as additional modifications including methylation, ubiquitination, succinylation, *O*-GlcNAcylation and others[14,51-53]; despite their abundance, these modifications are often studied in isolation. Our study examines the combinatorial landscape of tau phosphorylation in a physiological context to elucidate how its role is potentially disrupted in a pathological one.

While high levels of p-tau are most commonly described in the context of aggregates in disease, similar p-tau epitopes have been reported in a number of animal studies and recapitulated in our work here using PS19 mouse brains (**Fig. 1**). However, in the aged PS19 mouse, we found only a weak correlation between the relative abundance of a specific p-tau epitope and its presence in insoluble aggregates. For example, pS202/pT205

490 showed a large decrease in abundance in the aged brain compared to neonates but was strongly associated
491 with insoluble tau; conversely, pT212/pS214 showed a large increase in abundance but was also highly
492 associated with insoluble tau. Thus, while p-tau is generally enriched in insoluble fractions from aged PS19 mice,
493 this raises the intriguing possibility that combinatorial phospho-regulation rather than individual phospho-
494 epitopes may contribute to aggregation propensity in disease, as well as the extent to which phosphorylation at
495 some epitopes largely occurs after aggregate formation.

496 To provide more insight, we turned to iNeurons, which we demonstrate are a powerful system for the
497 study of endogenous tau phosphorylation both in the context of function and in disease. By top-down mass
498 spectrometry of iNeuron-derived tau, we showed that endogenous fetal tau is extensively phosphorylated, with
499 up to 21 phosphate groups per molecule – far exceeding prior estimates from fetal or AD brains[12,24,54,55].
500 Interestingly, a previous study similarly identified two pools of p-tau centered around ~8 and ~14 phosphates per
501 tau molecule, by utilizing 2N4R overexpression in insect cells[24]. However, in that study and in contrast to our
502 current work, the cells were pre-treated with phosphatase inhibitors prior to lysis to enrich p-tau; meanwhile, our
503 results support a natural higher level of p-tau in iPSC-derived human neurons.

504 The use of iNeurons allowed us to perturb MT stability chemically in order to measure dynamic alterations
505 to p-tau during MT destabilization and recovery. Importantly, we identified that specific combinations of phospho-
506 sites are co-regulated, shifting in response to changes in MT stability and growth cycles (**Fig. 7**). When MTs
507 destabilize, such as during the frequent collapse and regrowth cycles of axons, the first pool of p-tau species,
508 phosphorylated at S202/T205, T212 and T217, are dephosphorylated presumably to enhance tau's binding
509 capacity to tubulin/MTs. Then, a second pool of p-tau species (i.e., pT231, pS235, pS262) is dephosphorylated
510 to promote further MT stabilization. Based on our MT fractionation measurements for each phospho-epitope, the
511 rapid dephosphorylation of the first set of sites (S202/T205, T212 and T217) may indicate a cellular response to
512 increase the affinity of p-tau species which are already bound to MTs. Meanwhile, the slower dephosphorylation
513 of the second set of phospho-epitopes (T231, S235 and S262) may represent dephosphorylation of a
514 cytoplasmic fraction of tau, thus contributing to the overall population of dephosphorylated tau that is available
515 to promote MT growth and repair. Among the phospho-sites measured in this study, dephosphorylation at sites
516 T231, S235 and S262 appear to be the most critical for enhancing this interaction. Once MT stability is re-
517 established, these same sites are re-phosphorylated: first, epitopes S202/T205, T212 and T217 are
518 phosphorylated, possibly to facilitate dissociation of tau from MTs: then, tau is re-phosphorylated at sites that
519 strongly inhibit tau's binding to MTs (e.g., T231, S235 and S262) in order to maintain cytosolic pools of p-tau that
520 are dissociated from MTs.

521 This paradigm contrasts sharply with the prevailing view in neurodegeneration in which increased tau
522 phosphorylation is thought to drive MT destabilization. In fact, when we seeded iNeurons with human brain-
523 derived tau aggregates, we observed an abundant presence of tau aggregates and globally elevated p-tau levels
524 (**Fig. 2**), and thus a presumed loss of functional tau, but we did not detect a decrease in MT stability. Our findings
525 question the "tau cascade" of MT destabilization by suggesting a more nuanced relationship: in physiological
526 settings, tau phosphorylation responds to cytoskeletal changes and allows it to regulate MT stability, while in

527 disease, tau phosphorylation broadly still responds to cytoskeletal changes, but tau becomes sequestered in
528 aggregates and therefore is not available for function. In other words, tau may not simply stabilize MTs, but rather
529 may maintain dynamic MT instability, consistent with recent findings that tau enhances tubulin incorporation
530 preferentially at defect sites in the MT lattice[56].

531 Our data suggest, but do not prove, that depletion of soluble tau through aggregation impairs tau's ability
532 to counteract MT destabilization. In seeded neurons, we observed increased phosphorylation across most
533 epitopes tested, which was sustained at only a few sites during MT collapse, notably at epitopes S235 and S262.
534 These two epitopes are among the most disruptive to tau-MT interactions, are highly sensitive to PP2a activity,
535 and thus appear essential for regulating tau's ability to stabilize MTs. Consistent with this, PP2a inhibition in
536 unseeded neurons markedly blunted dephosphorylation at S235 and S262 during MT collapse, and resulted in
537 MT destabilization comparable to levels seen in AD-seeded neurons. Given that S235 and S262 lie within or
538 adjacent to the proposed fibril core of tau, reported by cryo-electron microscopy to span approximately residues
539 254-381 or more concisely from 306-378 (depending on the structural model)[57-60], its apparent inaccessibility
540 within aggregates may prevent normal PP2a-mediated dephosphorylation, locking tau in an elevated
541 phosphorylated state that is unable to respond to MT stress.

542 Our findings point to site-specific, combinatorial layers of phospho-regulation that govern tau's function.
543 Our prior work with recombinant tau and phospho-mimics led us to propose a model whereby the contributions
544 of individual phospho-modifications to disrupting interactions with MTs were relatively minor, but the
545 accumulation of multiple modifications could significantly disrupt function[16]. Our work here refines that model to
546 suggest that some individual phospho-sites are more disruptive than others are to MT-binding, but underscores
547 the importance of multiple modifications in fine-tuning tau-MT interactions in a biological setting. Many questions
548 remain about how combinatorial tau phosphorylation is regulated and how it influences tau's diverse functions.
549 Most of the pairwise and triplet phospho-combinations we identified are novel, leaving open how, when and
550 where these phospho-proteoforms arise in neurons, and what roles they play beyond regulating tubulin/MT
551 interactions. For example, we linked phosphorylation at S262 to phosphorylation at epitopes T212, T231, S235
552 and S396, all of which are highly abundant in AD brains[14]. Thus, the diversity of phospho-proteoforms may allow
553 tau to carry out distinct cellular roles, including MT regulation, tubulin-actin crosslinking, vesicle trafficking, or
554 synaptic modulation, depending on its modification profile.

555 Importantly, our study has limitations. Phospho-specific antibodies may vary in affinity and can be affected
556 by neighboring modifications, which may lead to underestimation of phospho-occupancy at certain sites. For
557 example, T181 phosphorylation frequently co-occurred with other phospho-sites while also exhibiting high levels
558 of independent phosphorylation, yet we likely underestimated its occupancy at only ~35%. Another limitation is
559 that the use of kinase/phosphatase inhibitors and cytoskeleton-targeting small molecules are non-specific, and
560 may affect tau indirectly, outside of physiological pathways that normally modify MT stability. Future work using
561 genetic approaches to modify trans-regulators of tau-MT interactions, high-resolution top-down proteomics or
562 genetic code-expansion strategies to incorporate site-specific PTMs, could more precisely resolve how phospho-
563 proteoforms are regulated and function.

564 In summary, our work reframes several central assumptions in the tau field. We demonstrate that while
565 single phospho-epitopes may be useful as biomarkers in tissue or CSF[5-8], they are poor predictors of tau
566 insolubility. Moreover, MT integrity can be maintained even in the presence of increased tau phosphorylation and
567 accumulation of aggregates. These insights were made possible by leveraging iNeurons as a model of
568 endogenous tau phosphorylation, allowing us to dissect combinatorial phospho-patterns in both healthy and
569 disease-relevant contexts. We propose a mechanistic link between combinatorial tau phosphorylation and an
570 impaired ability to counteract MT destabilization in the presence of tau aggregates, and that this phenotype is
571 strongly correlated with elevated phosphorylation at epitopes S235 and S262. Our findings reveal that
572 combinatorial tau phosphorylation patterns are tightly linked to MT dynamics and are organized in co-regulated
573 clusters that may foreshadow aggregation behavior in disease. These insights reframe our understanding of tau
574 regulation, emphasize the disruption caused by increased phosphorylation at S235 and S262 within tau
575 aggregates, and highlight new avenues for exploring how phosphorylation contributes to tau function and
576 dysfunction. Future studies may benefit from identifying specific phospho-proteoforms in physiological and
577 pathological contexts that could reveal tau molecules that are unique to the disease state.

578

579

580 # METHODS

581 ***Mouse lines and husbandry***

582 Ethical Statement: All animal procedures including husbandry and experimental procedures, were performed according to
583 NIH guidelines and approved by the Institutional Animal Care and Use Committee at Weill Cornell Medicine (Animal Welfare
584 Federal Wide Assurance No: A3290-01; protocol number 2014-0015).

585 Mouse strains: PS19 mice[61] overexpressing human tau (1N4R) carrying the disease-causing P301S mutation, driven by
586 the mouse prion protein promoter (stock# 008169, Jackson Lab, ME) and wildtype (C57BL/6 J; Stock # 000664 Jackson
587 Labs, ME) were kept in 12 h light/dark cycle in a temperature-controlled room with free access to water and food. PS19
588 transgenic mice (generated in C57BL/6 background, and inbred for >20 generations) were bred to wildtype mice of the
589 same line to generate 50% transgenic and 50% wildtype offspring used in this study. Littermates were raised together and
590 tissue were harvested in parallel.

591 ***Mouse tissue harvesting***

592 Mouse brains were dissected, washed once with ice-cold PBS, and cut into left and right hemispheres. The brains were
593 flash-frozen in under 60 seconds post-decapitation. For post-natal brain dissections, one hemisphere was immediately
594 flash-frozen in liquid nitrogen and stored at -80C for solubility assays. The other hemisphere was immediately resuspended
595 to 10% (w/v) in cold PBS supplemented with protease and phosphatase inhibitors, mechanically homogenized using a
596 dounce tissue grinder, and supplemented with 4x Laemmli buffer (supplemented with 10 mM DTT). The same
597 homogenization protocol was used for embryonic brain dissections (E12). These samples were stored at -80C to be used
598 for SDS-PAGE followed by immunoblot.

599 ***Primary neuron cultures***

600 Primary neurons from embryonic day 12 wildtype mice were cultured essentially as previously described[62]. Briefly, cortices

601 were dissected in ice-cold HBSS followed by trypsinization (0.05% trypsin-EDTA) for 10 min at 37 °C. The brains were then
602 triturated with a siliconized pipette and plated onto poly-L-lysine coated glass coverslips. Plating medium (DMEM, Thermo
603 Fisher) containing 5 g/L glucose, 0.2 g/L $NaHCO_3$, 0.1 g/L transferrin, 0.25 g/L insulin, 0.3 g/L L-glutamine, and 10% fetal
604 bovine serum was replaced with growth medium (DMEM, Thermo Fisher) containing 5 g/L glucose, 0.2 g/L $NaHCO_3$, 0.1
605 g/L transferrin, 0.3 g/L L-glutamine, 5% fetal bovine serum, 2% B-27 or N21-MAX supplement, and 2 μM cytosine
606 arabinoside 2 days after plating. On day *in vitro* 8, cultured neurons were washed twice with cold PBS and fixed with 4%
607 PFA (in PBS) for 20 minutes at room temperature, followed by immunofluorescence.

608 ***Generation of tau^{KD} human iPSCs***

609 Human WTC11 iPSCs stably-expressing Ngn2 (under a dox-inducible promoter) and dCas9-KRAB$_{(KOX1)}$ were transduced
610 with sgRNAs targeting *MAPT* followed by puromycin selection. Three sgRNAs were tested independently: 1)
611 5'GTGTTGGTGCCGGAGCTGGT, 2) 5'GGGCTGCAGTCGAGAGTGAA, and 3) 5'GGAAGCCCCAGTCTGCGGAG. Non-
612 targeting control (NTC) sgRNA: 5' GCCGAGCGGCAGGGTGCCGC. The first sgRNA resulted in stable knockdown of tau
613 protein for at least 45 days post-differentiation while the other two sgRNAs resulted in only partial tau knockdown. The
614 described experiments were performed using iPSCs generated from the first sgRNA, referred to as tau^{KD}.

615 ***Lentivirus production and transduction***

616 Lentivirus was generated as previously described[62]. Briefly, HEK293T cells were co-transfected at low passage with 1.06μg
617 of pMDLG (Addgene plasmid# 12251), 0.57μg of pMD2.G (Addgene plasmid# 12259), 0.4μg of pRSV-Rev (Addgene
618 plasmid# 12253) plasmid, and 1.6μg of the lentiviral plasmid, using 1:3 ratio of total DNA to PEI per well of a 6-well plate.
619 The culture medium was replaced after 6 hours with mTesR+ (for iPSC transductions) or neurobasal media (for neuronal
620 transductions). The supernatant was collected after 48h and passed through a 0.45 μM polyether sulfone filter to remove
621 any cell debris. Large batches of virus were made together and small aliquots were stored at -80°C, to be thawed only once.

622 iPSCs were transduced with lentivirus containing guides against *MAPT* or NTC followed by puromycin selection (1 μg/mL)
623 48 hours-post transduction for 72 hours (until control, non-transduced cells were 100% dead) to generate tau^{KD} iPSCs.

624 iPSC-derived tau^{KD} neural progenitors were transduced with lentivirus containing tau constructs at 72 hours post-
625 differentiation using the doxycycline-induced Ngn2 cassette. Neural progenitors were lifted with StemPro Accutase Cell
626 Dissociation Reagent (5 min, 37C), pelleted and resuspended in neuronal differentiation media. Neural progenitors were
627 plated at $0.5x10^6$ cells in a single well of a 6-well plate. Lentiviruses containing either FUW-0N3R^{myc} or FUW-0N3R^{EGFP} were
628 added to the media upon re-plating. We did not observe any silencing of exogenously expressed tau in differentiated
629 neurons using the UbC promoter.

630 ***iPSC culture and neuronal differentiation***

631 Human iPSC cultures and neuronal differentiation protocols were performed as previously described with minor
632 modifications[63]. CRISPRi-iPSCs expressing inducible Ngn2 from AAVS1 safe harbor locus were maintained in mTesR1+
633 media with mTesR1+ supplements. iPSCs were plated on hESC Matrigel and maintained in mTesR1+ media (Stem Cell
634 Technologies). iPSCs were differentiated to glutamatergic neurons following established protocols[63]. iPSCs were lifted and
635 singularized using StemPro Accutase (5 min, 37C) followed by neutralization with mTesR1+ media. Cells were gently
636 pelleted for 5 minutes at 300*g*, then resuspended to $0.7x10^6$ cells/mL in neuronal induction media: KnockOut DMEM/F-12
637 (Gibco# 12660012) + 1x NEAA (Gibco#11140050) + 1x GlutaMAX (Gibco# 35050-061) + 10 nM Y27632 ROCK inhibitor
638 (Tocris# 125410) + 1x N2 max (Gibco #17502-048) + 2 μg/mL doxycycline hydrochloride (Sigma# D9891). A complete media
639 change was made the following day using the same media. The next day, another complete media change was made but
640 without ROCK inhibitor. Neural progenitors were lifted and dissociated with StemPro Accutase 72-hours post neuronal

641 induction, pelleted (5 min, 300*g*), and re-plated at $0.5x10^6$ cells per well of a 6-well plate that was first coated overnight with
642 poly-L-ornithine hydrobromide (0.1 mg/mL in borate buffer pH 8.5; Sigma, #P3655). The replating maturation media
643 contained: Neurobasal-A (Gibco# 10888-022) + 1x NEAA + 1xGlutaMAX + 10 nM Y27632 ROCK inhibitor + 2 µg/mL
644 doxycycline hydrochloride + 1x B-27 plus (Gibco# A3582801) + CultureOne Supplement (Gibco #A3320201) + 10 ng/mL
645 BDNF (PeproTech #450-02) + 10 ng/mL NT-3 (PeproTech #450-03) + 1 µg/mL laminin (Gibco# 23017-015) + 200 µM L-
646 ascorbic acid (Sigma #A8960). 50% media changes were made every 7 days with the same media lacking ROCK inhibitor
647 and doxycycline. iNeurons were harvested at the time points indicated within each figure and figure legend.

648 WTC11 iPSC-derived neurons were used for all the experiments except for in tau seeding experiments ('Figure 2'), which
649 utilized KOLF2.1J iPSC-derived neurons. Differentiation protocols were essentially identical except the neural progenitor
650 phase was extended by an additional 4th day which was also supplemented with the anti-mitotic 5-fluorodeoxyuridine (5-
651 FdU).

652 ***Top-down mass spectrometry***

653 Top-down mass spectrometry (TD-MS) of tau proteoforms was performed essentially as previously described[64]. The
654 harvested iNeurons (8 million cells, DPI 30) were suspended in 500 µL of homogenization buffer composed of Ham's F12
655 medium supplemented with 1× Halt Protease and Phosphatase Inhibitor, 5 mM EDTA, and 0.45% CHAPS, and left in 4 °C
656 for half an hour for cell lysis. Afterwards, the cell lysate was subjected to sonication on ice for 20 seconds at 40% power,
657 using a pulse cycle of 2 seconds on and 3 seconds off. The lysate was then centrifuged at 17,000*g* for 30 minutes at 4°C
658 to separate cell debris, and supernatants were collected for tau IP. Tau antibody-conjugated beads were prepared by
659 incubating 10 µg each of HT-7 and Tau-5 antibodies with 50 µL of Protein A/G beads at room temperature for 10 minutes.
660 The prepared conjugated beads were added to 500 µL of the cell lysate and incubated overnight at 4°C with end-to-end
661 rotation. Afterwards, the beads were subjected to a series of wash steps: twice with 500 µL homogenization buffer, twice
662 with a 1:1 mixture of homogenization buffer and water, and three times with 500 µL of water. Finally, the tau proteins were
663 eluted from the beads incubation in 150 µL of 10% formic acid at room temperature for 30 minutes. The eluates were flash-
664 frozen and stored at -80 °C for further analysis.

665 Individual ion mass spectrometry (I^2MS) is an advanced top-down MS technique that enables direct mass readout of
666 complex tau proteoforms at the intact level[65]. The SampleStream platform (Integrated Protein Technologies) was interfaced
667 with a Q Exactive HF mass spectrometer (Thermo Fisher Scientific) using the Ion Max source equipped with a HESI II probe
668 to provide online buffer exchange and I^2MS analysis. Triplicate I^2MS runs were performed for the iNeuron-derived tau IP
669 sample. For each run, 50 µL of immunoprecipitated tau samples were cleaned and buffer-exchanged into a solution of 0.2%
670 (v/v) formic acid and 30% (v/v) acetonitrile in water, followed by direct injection into the mass spectrometer at a flow rate of
671 1.6 µL/min for I^2MS analysis. On the mass spectrometer, automated Ion Control (AIC) was utilized to dynamically adjust the
672 injection time based on ion signal density, ensuring optimal detection of individual ion signals. Additional mass spectrometry
673 settings included an Orbitrap central electrode voltage of 1 kV, trapping gas pressure of 0.3, m/z range of 650-2,500, a
674 resolution of 120,000 at m/z 200 (corresponding to a 1 s transient time), a spray voltage of 3.1 kV, in-source CID energy of
675 15 eV, and a source temperature of 320 °C. I^2MS data were acquired over a 50-minute period per run, totaling approximately
676 3,000 scans.

677 All the I^2MS transient files were converted to .storx files and processed using STORIboard
678 (https://www.proteinaceous.net/storiboard) with the voting charge assignment algorithm. After processing, .mzML files were
679 generated, presenting the mass domain spectrum of each run. The mass spectra were annotated by TDValidator
680 (Proteinaceous, https://www.proteinaceous.net/tdvalidator). Tau 0N3R proteoforms were matched to spectral peaks based

681 on intact mass, using a mass accuracy window of ±50 parts per million (ppm) and a mass tolerance of 1.8 Da. The 0N3R
682 proteoforms were quantified by their relative abundance.

683 ***SDS-PAGE and quantitative immunoblotting***

684 Proteins were separated by SDS-PAGE for immunoblotting as previously described[62]. Briefly, 8-15% Laemmli gels (10.3%T
685 and 3.3%C) were used to separate proteins on Bio-Rad apparati. 2.5 mM final DTT was used in SDS Laemmli buffer unless
686 indicated otherwise. Proteins were transferred onto nitrocellulose (pore-size = 0.45 µm; GE Healthcare) and blocked with
687 Every Blot Blocking Buffer (Bio-Rad). Immunoblotting was performed by incubating the blocked membranes with primary
688 antibodies in blocking buffer for overnight incubation. Following 5 washes with TBS-Tween 20 (0.1%), blots were incubated
689 with secondary antibodies (goat anti-rabbit conjugated to IRDye 680RD or 800CW; LI-COR) at 1/10,000 in blocking buffer
690 for 1-2 hours. Immunoblots were washed 5x with TBS-T and dried, then scanned on an Odyssey CLx (LI-COR) and
691 quantified using Image-Studio software (LI-COR).

692 ***Triton-X solubility assay of PS19 transgenic mouse brains***

693 Mouse brains from PS19 mice were dissected on ice at either post-natal day 0 or at 9-months. Brain lysates were subject
694 to Triton-X (Tx) solubility as previously described[66]. Briefly, brains were rinsed twice with ice cold PBS, then homogenized
695 in 0.1% Tx-100 in PBS supplemented with protease and phosphatase inhibitors. Samples were rotated for 30 min at 4C
696 and then sonicated 10x at 10% power (0.5 sec on, 1 sec off). The tissue was then centrifuged at 17,000*g* for 90 min at 4C.
697 The supernatant (soluble fraction) was collected, and the pellet (insoluble fraction) was resuspended in an equal volume of
698 lysis buffer as the supernatant. Each sample volume was doubled using 4x Laemmli buffer (supplemented with 10 mM DTT)
699 and sonicated again: 20x at 10% power (0.5 sec on, 1 sec off). The samples were then boiled at 95C for 20 min before
700 loading equal volumes of each fraction on SDS-PAGE, followed by immunoblot for tau. Approximately two-fold more tissue
701 levels were loaded for 9-month-old samples compared to neonates (as indicated by β-actin immunoblot) to improve
702 detection of lowly-detected phosphorylation epitopes, particularly at sites pS202/pT205, pT231 and pS262. Insoluble tau
703 was calculated as a percentage of total protein per sample and/or normalized to β-actin, as indicated.

704 ***0N3R recombinant aggregation and quantification***

705 Aggregation of 0N3R was prepared as previously described[67]. Briefly, 50 µM tau was supplemented with 500 µM DTT in a
706 sample volume of 100 µL of 1x PBS buffer, pH 7.4. The sample was then left on an IKA MS 3 control shaker with continuous
707 orbital shaking at 1000 rpm at 37C. Following a six-day aggregation period, the aggregates were pelleted by centrifugation
708 at 17,700*g* for 90 minutes. The supernatant was then separated from the pellet, and the pellet was resuspended to 100 µL.
709 The supernatant and pellet samples were boiled for 20 minutes and chilled on ice before an SDS-page gel was conducted
710 to calculate the approximate amount of protein in the pellet.

711 ***TEM Imaging***

712 The same tau 0N3R pellet was imaged using transmission electron microscopy (TEM) (Talos L120C TEM, ThermoFisher).
713 The fibrils (5 µL of 10 µM) were added to freshly glow-discharged carbon coated film 300 mesh grids (Electron Microscope
714 Sciences) and incubated for 1 minute. A wash with 5 µL water for 30s was performed to remove excess buffer salts. To
715 negative stain, the sample was incubated with 5 µL uranyl acetate (2% in water) for 1 minute. Between each step, excess
716 buffer was absorbed with filter paper. The grids were dried under vacuum pump for 2 minutes before imaging. The 0N3R
717 pellet sample was imaged with an accelerating voltage of 120 kV and a magnification of 22000x.

718 ***AD case selection and tau seeds extraction***

719 The AD patient was pathologically diagnosed as previously described[68]. The case was pathologically confirmed as late-

720 stage AD without comorbidities of Lewy body and TDP-43 pathologies based on immunohistochemical staining (data not
721 shown). Tau seeds were sequentially extracted from the frontal cortex using a previously described protocol[69]. Grey matter
722 and white matter were separated using a surgical blade, and only grey matter was used in the extractions. Brain homogenate
723 was prepared in nine volumes (v/w, mL/g) of PHF buffer (10 mM Tris, 10% sucrose, 0.8 M NaCl, 1 mM EDTA, pH 7.4) with
724 0.1% sarkosyl, proteinase inhibitor and phosphatase inhibitor in a glass dounce homogenizer and spun at 10,000*g* for 10
725 min at 4C. Supernatant (supernatant 1) was collected, sarkosyl was added to 1% final concentration, incubated in a beaker
726 with stirring for 1.5hr at RT, and followed by 150,000*g* spin for 75 min at 4C. The pellet was collected, briefly washed with
727 PBS to remove myelin, and resuspended in PBS (as pellet 1). To remove the sarkosyl, pellet 1 was spun at 150,000*g* for
728 75 min, and the resulting pellet was collected as pellet 2. Pellet 2 was resuspended in PBS, thoroughly sonicated, and spun
729 at 10,000*g* for 10 min at 4C. The supernatant was collected as the enriched tau seeds.

730 ***Tau seeding and aggregate detection***

731 Protocols for AD-derived tau seeds were adapted from previously established protocols[70]. KOLF2.1J-NGN2 iNeurons were
732 plated at either $0.2x10^6$ or $0.05x10^6$ cells per well for biochemistry or immunocytochemistry experiments, respectively. Three
733 weeks post-NGN2 induction, AD-derived seeds (0.1 µg/mL final) or recombinant 3R seeds (1.28 µg/mL final) were diluted
734 in 100 µL total of neuron maturation media. Seeds were sonicated on high in a temperature-regulated water bath for 20
735 minutes at 10C for pulses of 30 seconds on, 30 seconds off. The sonicated seeds were immediately transferred to ice and
736 further diluted to a total 720 µL in neuron maturation media. 20 µL of seed solution was added dropwise in a circular motion
737 to each treated well, triturated gently 5x, and then the plate was gently rocked back and forth. The seed solution was
738 triturated 5x between each treated well with a fresh tip. iNeurons were then maintained as described in the '*iPSC culture*
739 *and neuronal differentiation*' section using a 50% change of neuron maturation media with supplements (as indicated) every
740 7 days. For biochemistry experiments, iNeurons were treated at 4-weeks post-seeding with either DMSO or 10 µM
741 nocodazole for 90 minutes, as described in the '*Cytoskeleton manipulation by pharmacological reagents'* section.

742 ***Immunofluorescence in primary mouse neurons and iNeurons***

743 Immunofluorescence was performed essentially as previously described[62]. Cells were plated and maintained on tissue-
744 culture treated and coated glass coverslips (poly-L-laminin for primary neurons, poly-L-ornithine for iNeurons). Cells were
745 washed twice with PBS + 1 mM $MgCl_2$ and fixed in 4% paraformaldehyde (PFA) for 20 min at room temperature. The PFA
746 was washed out twice with PBS + 1 mM $MgCl_2$, then the cells were permeabilized for 5 minutes with 0.1% Tx-100 in PBS-
747 T, followed by incubation with blocking buffer (PBS-T + 5% BSA) for 1 hour at room temperature. Cells were incubated
748 overnight at 4C in primary antibody: β-tubulin III rabbit polyclonal (1:250), β-tubulin III mouse monoclonal (1:250), α-tubulin
749 1a mouse monoclonal (1:250), detyrosinated α-tubulin rabbit polyclonal (1:250).

750 For seeding experiments, iNeurons were fixed in ice-cold methanol at -20C for 15 minutes to extract soluble proteins,
751 followed by 1 hour incubation with blocking buffer (3% BSA and 3% goat serum), followed by overnight anti-AT8 (1:1000)
752 staining at 4C for detection of p-tau aggregates, or anti-β-tubulin III mouse monoclonal (1:250) for detection of polymerized
753 tubulin.

754 ***Pharmacological reagents***

755 The following pharmacological reagents were utilized throughout this study: Nocodazole (10 µM final; 12-281-0),
756 demecolcine (1 µM final; D7385; lot #102753904), paclitaxel (10 µM final; T1912; lot #1003615845), latrunculin A (2 µM
757 final; L5163; lot #0000373456), LB-100 (20 µM final; 29105; lot #0613520-17), Calyculin A (20 nM final; C5552; lot
758 #0000366393), AKT1 inhibitor VIII (20 µM final; 14870; lot #0613313-34), Erk1/2 inhibitor I (10 nM final; A1176841; lot
759 #HA2), GSK3β BIO-1 inhibitor (5 µM final; 13123; lot #0586619-49).

760 ***Cytoskeleton manipulation by pharmacological reagents***

761 iNeurons (*DPI 21*) were treated with either DMSO, nocodazole (10 μM), demecolcine (1 μM), paclitaxel (10 μM) or latrunculin
762 A (2 μM) for 90 minutes in complete neuronal media. Cells were washed twice with PBS at room temperature and harvested
763 for Western blot in ice-cold RIPA buffer supplemented with protease and phosphatase inhibitors.

764 ***Pharmacological microtubule catastrophe by nocodazole treatment***

765 Nocodazole was resuspended in DMSO to 10 mM, aliquoted and stored at -20C. DPI 25 iNeurons ($0.5x10^6$ per well of a 6-
766 well plate for immunoblot, $0.4x10^5$ per well of a 24-well plate for immunofluorescence) were washed once with ice-cold PBS
767 for 5 min to facilitate MT catastrophe, and then treated with 10 μM nocodazole (final) in pre-warmed complete neuronal
768 media for either 15 minutes or 90 minutes at 37C. For MT recovery experiments, nocodazole was washed out by aspirating
769 out the media and performing three washes with pre-warmed neuronal media without nocodazole. After the third wash was
770 removed, the cells were incubated at 37C in complete neuronal media without nocodazole for either 1 hour, 3 hours or 6
771 hours to allow for MT recovery. At the final time point, for immunoblot, the cells were washed twice with room temperature
772 PBS then lysed and scraped in ice-cold RIPA buffer supplemented with protease inhibitors and phosphatase inhibitors on
773 ice. Following 10 min of rotation at 4C, debris were pelleted at 17,000*g* for 10 min at 4C, the supernatant was collected and
774 supplemented with 4x Laemmli buffer + 10 mM DTT, boiled for 20 min at 95C, then subject to SDS-PAGE followed by
775 immunoblot. For immunofluorescence, the cells were washed twice with 0.1M PHEM buffer (pH 7.2) at room temperature
776 and fixed for 15 min in 4%PFA/0.25%GA in 0.1M PHEM buffer (pH 7.2) at room temperature. The fixative was washed out
777 3x with PHEM buffer, and immunofluorescence was performed as described above except PBS was replaced with PHEM
778 buffer for all steps including washing and blocking buffer (5% BSA in PHEM-T). Stable microtubules were detected by anti-
779 acetylated α-tubulin and anti-detyrosinated α-tubulin antibodies.

780 ***Kinase/phosphatase inhibition***

781 iNeurons (*DPI 30*) were treated for 90 minutes with nocodazole (10 μM) and either LB-100 (20 μM) or Calyculin A (20 nM).
782 Cells were either washed and collected for Western blot at this point, or the nocodazole and phosphatase inhibitors were
783 washed out 3x with pre-warmed complete media (lacking nocodazole and phosphatase inhibitors) and allowed to recover
784 at 37C for 3 hours prior to harvesting. For kinase inhibition, neurons were treated for 90 minutes with 10 μM nocodazole
785 followed by 3x washout, followed by incubation with AKT1 inhibitor VIII (20 μM) for 3 hours at 37C. At this final timepoint,
786 cells were then harvested, as described above, for Western blot.

787 ***Intact microtubule fractionation from iNeurons***

788 Intact microtubules were fractionated from soluble cytosolic proteins using tau^{KD} iNeurons expressing FUW-0N3R^{myc} at 12
789 days post-neuronal induction following established protocols[71]. Neurons were plated at $0.5x10^6$ cells in a single well of a
790 12-well PLO-coated plate.

791 Fresh microtubule stabilization buffer (MSB) was made containing 100 mM PIPES (Millipore Sigma #P1851) + 1 mM $MgSO_4$
792 (M2643) + 2 mM EGTA (E3889) + 0.1 mM EDTA (E8008) + 2 M glycerol (G9012). The pH was adjusted to 6.75 with KOH
793 (221473) to fully dissolve the PIPES. 1 mM PMSF (10837091001) + 1x protease inhibitor (P8340) + 1x Halt phosphatase
794 inhibitor cocktail (78420) were added fresh immediately before the assay. MSB was pre-warmed to 37C.

795 The media was aspirated, and the cells were gently washed once with MSB. Next, the cells were incubated with 300 μL of
796 pre-warmed MSB containing 1% Tx-100 for 5 min at 37C. The plate was gently tilted after the addition of the buffer. After 5
797 minutes, the buffer was collected (and placed on ice) and the cells were washed with 300 μL of the same buffer and
798 combined with the initial collection, termed the cytosolic fraction. Cells with intact cytoskeletons remained adhered to the

799 well. These were scraped in 600 µL MSB containing 1% Tx-100 and placed on ice (intact MT fraction). Following the
800 extractions, the two fractions were brought to equivalent volumes in MSB + 1% Tx-100. 200 µL 4X Laemmli SDS loading
801 buffer (supplemented with 10 mM DTT) was added to each sample. Samples were boiled for 20 min at 95C and immediately
802 subject to separation by SDS-PAGE for immunoblot.

803 The same protocol was used for immunofluorescence except cells were either incubated for 5 min at 37C in MSB (no
804 cytosolic extraction) or MSB + 1% Tx-100 (cytosolic extraction), followed by a single wash in the same buffer and then
805 fixation by 4% PFA in PBS for 20 min at room temperature.

806 Anti-detyrosinated α-tubulin was used as a marker for intact MTs, and anti-NSE was used as a cytosolic/membrane marker.

807 ***Purification of recombinant tau wildtype and phospho-mimic proteins***

808 Recombinant tau proteins were expressed in BL21(DE3) cells and purified as previously described with minor
809 modifications[16]. *MAPT* was cloned into the pET-HT vector with a N-terminal 6xHis-TEV fusion, and transformed into
810 BL21(DE3) competent cells. Overnight starter cultures were incubated in 500 mL LB broth at 37C until OD600=0.6, at which
811 time protein expression was induced with 1 mM isopropyl-β-D-1-thiogalactopyranoside (IPTG) at 18C for 16 hours. Bacteria
812 were then pelleted (4000*g* for 20 min at 4C) and resuspended in cold lysis buffer (20 mM Tris pH 8.0, 150 mM NaCl, 1
813 Roche EDTA-free protease inhibitor tablet, 1 mg/mL lysozyme, 20 mM imidazole, 1 mM PMSF, 1x DNase, 1 mM $MgCl_2$).
814 Cells were rotated at 4C for 30 minutes followed by sonication on ice (2 minutes; 1 sec on, 2 sec off) and centrifuged again
815 (20,000*g*, 30 minutes at 4C) to remove cellular debris. The supernatant was subject to affinity capture using Ni-NTA resin
816 (Fisher; PI88222) for 1 hour, rotating, at 4C. Unbound proteins were washed away with 6 column volumes of buffer
817 containing 20 mM Tris pH 8.0 + 150 mM NaCl + 20 mM imidazole, then eluted in the same buffer containing 300 mM
818 imidazole. The eluted 6xHis-TEV-tau protein was buffer exchanged to the previous buffer (20 mM Tris pH 8.0 + 150 mM
819 NaCl + 20 mM imidazole) using a 10 kDa MWCO Amicon Ultra-15 Centrifugal Filter Unit (Millipore #UFC9010), concentrated
820 to ~1.5 mL, and incubated with super TEV protease-6xHis (1:300 enzyme to tau molar ratio) and 1 mM DTT, rotating at 4C
821 overnight. The following day, the mixture was diluted 15-fold in 20 mM Tris pH 8.0 + 150 mM NaCl + 20 mM imidazole to
822 dilute the DTT and reverse-Ni NTA affinity capture (1 hour, rotating at 4C) was used to remove the TEV-6xHis protease from
823 the mixture. The flowthrough (containing tau) was collected and buffer exchanged into 20 mM Tris pH 8.0 + 150 mM NaCl
824 + 1 mM EDTA + 1 mM TCEP, concentrated to ~2 mL and injected onto a HiLoad 16/600 Superdex 200 PG column for size
825 exclusion in the same buffer. Fractions containing tau were identified by UV-absorption at 280 nm. Fractions containing
826 >95% pure tau were pooled, concentrated to ~100 µM (determined by NanoDrop), aliquoted, flash frozen in liquid N_2 and
827 stored at -80C to be used for a single freeze-thaw cycle.

828 Tau phospho-mimic mutation sequences are as follows: Thr181Glu (ACA>GAA): Thr217Glu (ACC>GAA): Thr231Glu
829 (ACT>GAA): Ser235Glu (TCG>GAG): Ser262Glu (TCC>GAA): Ser396Glu (TCG>GAG): Ser404Glu (TCT>GAA).

830 ***Purification of tubulin from bovine brains***

831 Tubulin was purified from fresh bovine brains as previously described[72] and flash frozen in BRB80 buffer (80 mM PIPES +
832 1 mM $MgCl_2$ + 1 mM EGTA, pH 6.8). Frozen aliquots were thawed on ice and clarified by centrifugation at 100,000*g* for 6
833 min at 4C. The supernatant was collected, and the concentration of tubulin was estimated using NanoDrop. Clarified
834 samples were used immediately for the MT polymerization assay, and fresh aliquots were clarified for each replicate.

835 ***Microtubule polymerization assay by turbidity***

836 Polymerization of tubulin was monitored by light scatter at 340 nm as previously described with minor adjustments[15]. Freshly
837 clarified tubulin (20 µM final) was incubated with tau protein (10 µM final) in cold BRB80 buffer supplemented with fresh 1

838 mM DTT. A 250 µL reaction was made on ice and 100x fresh GTP (1 mM final) was added and mixed by pipette trituration
839 on ice. After 5 minutes, 200 µL were quickly transferred to a pre-warmed 96-well black-walled clear bottom plate and the
840 reaction was monitored at 37C for 45 minutes on a M1000 Tecan spectrophotometer. 9 flash measurements were made
841 and averaged per well per timepoint throughout the kinetic measurement. Each replicate of 0N3R tau wildtype and phospho-
842 mimics were measured in parallel. Three independent measurements were made and compared to their respective wildtype
843 measurements for each sample, to account for read-to-read variability. Afterwards samples were returned to ice for 5 min
844 to confirm that the samples could be depolymerized (thus eliminating concern for potential protein aggregation).
845 Polymerization curves were corrected by subtracting a plate blank, a buffer blank and a tubulin + GTP (no tau) measurement
846 from each sample. Curves were then normalized to the maximum data point for each sample. The time to 50% V_{max} was
847 compared to wildtype for each isoform and averaged for final measurements.

848 ***Immunoprecipitation of phospho-tau***

849 Tau^{KD} iNeurons were re-plated at $2x10^7$ cells/plate on a PLO-coated 15-cm dish and transduced with FUW-0N3R^{EGFP}. At 32
850 days post-induction, iNeurons were washed twice with room temperature PBS and then harvested in the dish in 8 mL of
851 ice-cold RIPA buffer (supplemented with 2x protease inhibitors and 2x phosphatase inhibitors). The cells were transferred
852 to a conical tube and rotated at 4C for 10 minutes, followed by pelleting of debris by centrifugation at 17,000*g* for 10 min at
853 4C. The supernatant was collected and divided into 8 equal tubes (1 mL each, ~$2.5x10^6$ cells per tube) for phospho-tau
854 immunoprecipitation. 50 µL of lysate was collected from each tube and was supplemented with 50 µL of 4x Laemmli buffer
855 (supplemented with 100 mM DTT, and boiled for 15 min at 95C before SDS-PAGE) for the input lanes. Phospho-tau
856 antibodies were added to the remaining lysates and rotated at 4C overnight: pT181 mouse monoclonal (10µg), AT8 mouse
857 monoclonal (10µg), pT212 rabbit polyclonal (10µg), pT217 rabbit polyclonal (10µg), pT231 mouse monoclonal (10µg),
858 pS235 mouse monoclonal (15µg), pS396 rabbit polyclonal (5µg) or non-specific mouse or rabbit IgG (for IgG control). The
859 following morning, either Protein A (Neta/Sigma, GE28-9513-78) or Protein G (Neta/Sigma, GE28-9513-79) magnetic
860 sepharose beads were washed 3x with ice-cold RIPA buffer and incubated with each immunoprecipitation for 2 hours,
861 rotating at 4C. The beads were then gently pelleted and washed 3x with ice-cold RIPA buffer using a DynaMag-2 Magnet
862 rack (Fisher, 12-321-D). Affinity captured proteins were eluted into 170 µL of 2x Laemmli buffer (supplemented with 50 mM
863 DTT) at 95C for 15 minutes. Samples were subject to SDS-PAGE followed by co-blotting for phospho-tau epitopes.

864 ***Calculation of phospho-tau abundance and co-occurrence***

865 Affinity-captured phospho-tau was assumed to be monomeric and soluble due to the presence of deoxycholate, triton-X
866 and SDS in the lysis and wash buffers, and therefore co-blotted phospho-tau was assumed to be covalently-modified tau
867 rather than the result of tau multimerization. Volumes per well for each measurement for SDS-PAGE: input (5µL,
868 representative of ~$6.25x10^3$ cells, or 2.24% of the IP lane), IgG control or eluted phospho-tau (20µL, representative of
869 ~$2.79x10^5$ cells). Signal intensities in the input lane were back-calculated to 100% of the IP lane (by multiplication by 44.7.

870 <u>*To calculate phospho-tau abundance*</u>

871 The efficiency of phospho-tau that was affinity-captured by each phospho-specific antibody was calculated using
872 immunoblot:

873 A. Efficiency of phospho-tau capture = Intensity of p-tau IP lane / Back-calculated intensity of p-tau input lane.

874 Next, the percentage of total tau that was recovered within each affinity capture was calculated. This number represents
875 the percentage of phospho-tau that was recovered from the total tau lysate.

876 B. Efficiency of total tau capture = Intensity of total tau IP lane / Back-calculated intensity of total tau input lane.

877 Lastly, phospho-tau abundance was estimated by using a ratio of 'B / A'. In other words, of the A% of phospho-tau that was
878 recovered, B% of it was positive for the given phospho-tau epitope. For example, for a given replicate, if 2.57% of pT181
879 was recovered ('A'), and this was equal to 1.03% of total tau recovery ('B'), then 'B / A' = 1.03% / 2.57% = 39.9% of total tau
880 is phosphorylated at T181. Abundance was calculated using the average of a technical repeat for each replicate, and then
881 averaged across all replicates: pT181 (n=4), AT8 (n=5), pT212 (n=4), pT217 (n=6), pT231 (n=6), pS235 (n=6), pS396 (n=4).

882 *To calculate phospho-tau co-occurrence*

883 The same logic as above was used to calculate phospho-tau co-occurrence:

884 C. Efficiency of phospho-tau co-occurrence = Intensity of p-tau co-blot in IP lane / Back-calculated intensity of co-
885 blotted p-tau in input lane.

886 Co-occurrence was calculated using a ratio of 'C / A'. In other words, of the A% of phospho-tau that was recovered, C% of
887 it was positive for the given co-occurring phospho-tau epitope. For example, for a given replicate if 0.052% of AT8 was
888 recovered ('C') from the pT181 immunoprecipitation (A = 2.57%), then 'C / A' = 0.052% / 2.57% = 20.1% of pT181 molecules
889 carry a phospho-modification at the AT8 epitope.

890 Recovery of tau phosphorylated at Ser235 was too inefficient to reliably quantify co-occurrence of phosphorylation;
891 therefore, these calculations were omitted.

892 Combinations of three co-occurring phospho-epitopes were predicted by minimum linkage analysis, which ranks trios based
893 on their weakest link by accounting for co-occurrence in both directions. In other words, low P(A, B) will penalize the score
894 even if P(A, C) + P (B, C) is high.

895 ***Antibody list***

Antibody	Host Species	Manufacturer	Catalog #	Working Dilution
Tau5 (pan-tau)	Mouse	Invitrogen	MA5-12808	1:1000 (WB)
Tau5 (pan-tau)	Rabbit	Novus	NB015844	1:1000 (WB)
HT7 (pan-tau)	Mouse	Invitrogen	MN1000	For IP only
AT270 (Tau pT181)	Mouse	Invitrogen	MN1050	1:1000 (WB)
AT8 (Tau pS202/pT205)	Mouse	Invitrogen	MN1020	1:1000 (WB) 1:1000 (ICC)
Tau pT212	Rabbit	Invitrogen	44740G	1:1000 (WB)
Tau pS214	Rabbit	Invitrogen	44742G	1:500 (WB)
AT100 (Tau pT212/pS214)	Mouse	Invitrogen	MN1060	1:1000 (WB)
Tau pT217	Rabbit	Invitrogen	44-744	1:1000 (WB)
AT180 (Tau pT231)	Mouse	Invitrogen	MN1040	1:1000 (WB)
Tau pS235	Mouse	Millipore Sigma	MABN2275	1:500 (WB)
Tau pS262	Rabbit	Invitrogen	44-750G	1:500 (WB)
Tau pS324	Rabbit	Abcam	ab109404	1:500 (WB)
Tau pS356	Rabbit	Invitrogen	44-751G	1:500 (WB)
Tau pS396	Rabbit	Invitrogen	44-752G	1:1000 (WB)
Tau pS404	Rabbit	Invitrogen	44-758G	1:1000 (WB)
Tau pS416	Rabbit	Invitrogen	PA1-4719	1:1000 (WB)
Tau pS422	Rabbit	Invitrogen	44-764G	1:1000 (WB)
NeuN	Rabbit	Invitrogen	PA5-74899	1:1000 (WB)
GAPDH	Rabbit			1:1000 (WB)
Tau 3R	Mouse	Millipore Sigma	05803MI	1:1000 (WB)
β-tubulin III	Mouse	R&D Systems	MAB1195	1:1000 (WB) 1:250 (ICC)
β-tubulin III	Rabbit	Invitrogen	PA5-86069	1:250 (ICC)
α-tubulin 1A	Rabbit	Abcam	ab18251	1:1000 (WB)
Detyrosinated α-tubulin	Rabbit	Millipore Sigma	AB3201	1:1000 (WB) 1:250 (ICC)

Acetylated α-tubulin (aK40)	Mouse	Invitrogen	6-11B-1	1:1000 (WB)
β-actin	Mouse	Invitrogen	MA1-744	1:1000 (WB)
Hsp70	Mouse	Invitrogen	MA3-007	1:250 (WB)
NSE	Rabbit	Abcam	ab53025	1:1000 (WB)
MAP1A	Rabbit	Invitrogen	PA558642	1:1000 (WB)
MAP1B	Rabbit	Invitrogen	PA578052	1:1000 (WB)
MAP2	Rabbit	Millipore Sigma	AB5622	1:1000 (WB)
SV2a	Rabbit	Thermo Fisher	PA5-115990	1:1000 (WB)
pAkt1 (pS473)	Rabbit	Invitrogen	44621G	1:500 (WB)
Akt1	Mouse	Invitrogen	AHO1112	1:250 (WB)
pErk1/2 (pT202/pT204)	Mouse	Invitrogen	501128621	1:1000 (WB)
Erk1/2	Rabbit	Invitrogen	MA515134	1:1000 (WB)
pGSK3β (pY216)	Rabbit	Invitrogen	44604G	1:1000 (WB)
GSK3β	Mouse	Invitrogen	MA515597	1:1000 (WB)
Methyl-PP2a (mL309)	Mouse	Santa Cruz	sc-81603 (2A10)	1:200 (WB)
pPP2a (pY307)	Rabbit	Invitrogen	PIPA536874	1:500 (WB)
PP2a	Rabbit	Invitrogen	PA517510	1:1000 (WB)
VDAC1	Mouse	Millipore Sigma	MABN504	1:2000 (WB)

Anti-tau antibodies were knockout/knockdown validated using either mouse brains, iPSC-derived neurons or both. Anti-pS422 had a strong, non-specific band at ~50 kDa, slightly beneath a faint p-tau band, in iPSC-derived neurons but not in mouse brains. The non-specific signal occluded reliable quantification in iNeurons. AT100 (pT212/pS214) was not detected in iNeurons, and in concurrence anti-pS214 (Invitrogen, #44742G) was inconsistently detected as a very faint band that could not be reliably quantified.

Statistical analysis

All experiments were performed using reagents that were aliquoted to minimize freeze-thaw cycles and improve reproducibility. Each 'n' was collected independently, as indicated in the figure legends. SC randomized and blinded NNN to sample identifies (lentivirus identities, mouse ages, sample treatments) for data analysis. All analyses were performed using PyCharm Community Edition 2023.2.4. Statistical significance for comparisons between two sample groups was determined by two-tailed Student's *t* test. Significance for curve comparisons for nocodazole-treated sample groups was determined by post-hoc Tukey's HSD test. Significance for curve comparisons for MT polymerization reactions was determined by two-way ANOVA analysis.

ACKNOWLEDGEMENTS

This work was supported by funding to N.N.N. (F31NS098623, F32AG079537, K99AG084855, AARF-22-924146), to E.R. (RF1AG053951), to O.S. (DP2-GM137416, Target ALS, Chan-Zuckerberg Institute), to M.S. (R01AG083949, R01NS095988, R01AG052505), to N.L.K. (P30CA060553 and P41GM108569), to E.B.L. (P30AG072979, P01AG066597) and to Virginia M. Lee (R01AG076434).

AUTHOR INFORMATION

AUTHORS AND AFFILIATIONS

Department of Chemistry, University of Pennsylvania, Philadelphia, PA, USA

Nima N Naseri, Ibrahim Saleh, Elizabeth Rhoades

Center for Cellular and Molecular Therapeutics, Children's Hospital of Philadelphia, Philadelphia, PA, USA

Nima N Naseri, Sapanna Chantarawong, Ophir Shalem

Department of Chemistry, Northwestern University, Evanston, Illinois 60208, United States

Tian Xu, Steven M Patrie, Neil L Kelleher

Appel Institute for Alzheimer's Research, and Feil Family Brain & Mind Research Institute, Weill Cornell Medicine, New York, NY, USA

Manu Sharma

Department of Pathology and Laboratory Medicine, Perelman School of Medicine, University of Pennsylvania, Philadelphia, PA, USA

Edward B Lee, Hong Xu

Department of Genetics, Perelman School of Medicine, University of Pennsylvania, Philadelphia, PA, USA

Ophir Shalem

Department of Biochemistry & Biophysics, Perelman School of Medicine, University of Pennsylvania, Philadelphia, PA, USA

Elizabeth Rhoades

CONTRIBUTIONS

NNN and ER conceived the project, directed by ER and OS. All experiments were performed and analyzed by NNN unless otherwise indicated. TX performed top-down mass spectrometry experiments under guidance by SMP and NLK. IS generated recombinant 3R tau seeds and performed TEM imaging. We thank Polina Holubovska for providing recombinant 0N3R tau for generating recombinant seeds. SC provided technical support. MS provided mice. EBL and HX provided AD-derived tau seeds and seeding protocols.

CORRESPONDING AUTHOR

Correspondence to Elizabeth Rhoades.

ETHICS DECLARATIONS

The authors declare no competing interests.

DATA AVAILABILITY

The raw immunoblots generated in this study are available in the supporting information.

REFERENCES

1 Brion, J., Passareiro, H., Nunez, J. & Flament-Durand, J. Mise en evidence immunologique de la proteine tau au niveau des lesions de degenerescence neurofibril-laire de la maladie d'Alzheimer. *Arch Biol (Bruxelles)* **95**, 229-235 (1985).

2 Grundke-Iqbal, I. *et al.* Abnormal phosphorylation of the microtubule-associated protein tau (tau) in Alzheimer cytoskeletal pathology. *Proc Natl Acad Sci U S A* **83**, 4913-4917 (1986).

3 Ihara, Y., Nukina, N., Miura, R. & Ogawara, M. Phosphorylated tau protein is integrated into paired helical filaments in Alzheimer's disease. *The Journal of Biochemistry* **99**, 1807-1810 (1986).

4 Lövestam, S. *et al.* (eLife Sciences Publications, Ltd, 2025).

5 Thijssen, E. H. *et al.* Plasma phosphorylated tau 217 and phosphorylated tau 181 as biomarkers in Alzheimer's disease and frontotemporal lobar degeneration: a retrospective diagnostic performance study. *Lancet Neurol* **20**, 739-752 (2021). https://doi.org:10.1016/s1474-4422(21)00214-3

6 Janelidze, S. *et al.* Plasma P-tau181 in Alzheimer's disease: relationship to other biomarkers, differential diagnosis, neuropathology and longitudinal progression to Alzheimer's dementia. *Nature medicine* **26**, 379-386 (2020). https://doi.org:10.1038/s41591-020-0755-1

7 Brickman, A. M. *et al.* Plasma p-tau181, p-tau217, and other blood-based Alzheimer's disease biomarkers in a multi-ethnic, community study. *Alzheimers Dement* **17**, 1353-1364 (2021). https://doi.org:10.1002/alz.12301

8 Palmqvist, S. *et al.* Blood Biomarkers to Detect Alzheimer Disease in Primary Care and Secondary Care. *JAMA* **332**, 1245-1257 (2024). https://doi.org:10.1001/jama.2024.13855

9 Pope, W. *et al.* Phosphorylated tau epitope of Alzheimer's disease is coupled to axon development in the avian central nervous system. *Experimental neurology* **120**, 106-113 (1993).

10 Yu, Y. *et al.* Developmental regulation of tau phosphorylation, tau kinases, and tau phosphatases. *Journal of Neurochemistry* **108**, 1480-1494 (2009). https://doi.org:10.1111/j.1471-4159.2009.05882.x

11 Hefti, M. M. *et al.* Tau phosphorylation and aggregation in the developing human brain. *Journal of Neuropathology & Experimental Neurology* **78**, 930-938 (2019).

12 Kenessey, A. & Yen, S. H. The extent of phosphorylation of fetal tau is comparable to that of PHF-tau from Alzheimer paired helical filaments. *Brain Res* **629**, 40-46 (1993). https://doi.org:10.1016/0006-8993(93)90478-6

13 Andreadis, A. Tau gene alternative splicing: expression patterns, regulation and modulation of function in normal brain and neurodegenerative diseases. *Biochimica et biophysica acta* **1739**, 91-103 (2005). https://doi.org:10.1016/j.bbadis.2004.08.010

14 Wesseling, H. *et al.* Tau PTM Profiles Identify Patient Heterogeneity and Stages of Alzheimer's Disease. *Cell* **183**, 1699-1713.e1613 (2020). https://doi.org:10.1016/j.cell.2020.10.029

15 McKibben, K. M. & Rhoades, E. Independent tubulin binding and polymerization by the proline-rich region of Tau is regulated by Tau's N-terminal domain. *The Journal of biological chemistry* **294**, 19381-19394 (2019). https://doi.org:10.1074/jbc.RA119.010172

16 Acosta, K. *et al.* Structural insights into the role of the proline rich region in tau function. *Structure* (2025).

17 Sengupta, A. *et al.* Phosphorylation of tau at both Thr 231 and Ser 262 is required for maximal inhibition of its binding to microtubules. *Arch Biochem Biophys* **357**, 299-309 (1998). https://doi.org:10.1006/abbi.1998.0813

18 Goode, B. L. *et al.* Functional interactions between the proline-rich and repeat regions of tau enhance microtubule binding and assembly. *Molecular biology of the cell* **8**, 353-365 (1997).

19 Preuss, U., Biernat, J., Mandelkow, E.-M. & Mandelkow, E. The 'jaws' model of tau-microtubule interaction examined in CHO cells. *Journal of cell science* **110**, 789-800 (1997).

20 Brotzakis, Z. F. *et al.* A structural ensemble of a tau-microtubule complex reveals regulatory tau phosphorylation and acetylation mechanisms. *ACS Central Science* **7**, 1986-1995 (2021).

21 Kellogg, E. H. *et al.* Near-atomic model of microtubule-tau interactions. *Science (New York, N.Y.)* **360**, 1242-1246 (2018).

22 Schwalbe, M. *et al.* Structural Impact of Tau Phosphorylation at Threonine 231. *Structure* **23**, 1448-1458 (2015). https://doi.org:https://doi.org/10.1016/j.str.2015.06.002

23 Alonso, A. d. C. *et al.* Interaction of tau isoforms with Alzheimer's disease abnormally hyperphosphorylated tau and in VitroPhosphorylation into the disease-like protein. *Journal of Biological Chemistry* **276**, 37967-37973 (2001).

24 Drepper, F. *et al.* A combinatorial native MS and LC-MS/MS approach reveals high intrinsic phosphorylation of human Tau but minimal levels of other key modifications. *Journal of Biological Chemistry* **295**, 18213-18225 (2020).

25 Stefanoska, K. *et al.* Alzheimer's disease: Ablating single master site abolishes tau hyperphosphorylation. *Science advances* **8**, eabl8809 (2022).

26 Singh, T. J., Grundke-Iqbal, I. & Iqbal, K. Differential phosphorylation of human tau isoforms containing three repeats by several protein kinases. *Arch Biochem Biophys* **328**, 43-50 (1996). https://doi.org:10.1006/abbi.1996.0140

27 Cho, J.-H. & Johnson, G. V. W. Glycogen Synthase Kinase 3β Phosphorylates Tau at Both Primed and Unprimed Sites: DIFFERENTIAL IMPACT ON MICROTUBULE BINDING *. *Journal of Biological Chemistry* **278**, 187-193 (2003). https://doi.org:10.1074/jbc.M206236200

28 Li, T., Hawkes, C., Qureshi, H. Y., Kar, S. & Paudel, H. K. Cyclin-Dependent Protein Kinase 5 Primes Microtubule-Associated Protein Tau Site-Specifically for Glycogen Synthase Kinase 3β. *Biochemistry* **45**, 3134-3145 (2006). https://doi.org:10.1021/bi051635j

29 Islam, T. *et al.* Phospho-tau serine-262 and serine-356 as biomarkers of pre-tangle soluble tau assemblies in Alzheimer's disease. *Nature medicine*, 1-15 (2025).

30 Haj-Yahya, M. *et al.* Site-specific hyperphosphorylation inhibits, rather than promotes, tau fibrillization, seeding capacity, and its microtubule binding. *Angewandte Chemie International Edition* **59**, 4059-4067 (2020).

31 Augustinack, J. C., Schneider, A., Mandelkow, E. M. & Hyman, B. T. Specific tau phosphorylation sites correlate with severity of neuronal cytopathology in Alzheimer's disease. *Acta Neuropathol* **103**, 26-35 (2002). https://doi.org:10.1007/s004010100423

32 Schneider, A., Biernat, J., von Bergen, M., Mandelkow, E. & Mandelkow, E. M. Phosphorylation that Detaches Tau Protein from Microtubules (Ser262, Ser214) Also Protects It against Aggregation into Alzheimer Paired Helical Filaments. *Biochemistry* **38**, 3549-3558 (1999). https://doi.org:10.1021/bi981874p

33 Hempen, B. & Brion, J.-P. Reduction of acetylated α-tubulin immunoreactivity in neurofibrillary tangle-bearing neurons in Alzheimer's disease. *Journal of Neuropathology & Experimental Neurology* **55**, 964-972 (1996).

34 Cash, A. D. *et al.* Microtubule reduction in Alzheimer's disease and aging is independent of τ filament formation. *The American journal of pathology* **162**, 1623-1627 (2003).

35 Qiang, L., Yu, W., Andreadis, A., Luo, M. & Baas, P. W. Tau protects microtubules in the axon from severing by katanin. *The Journal of neuroscience : the official journal of the Society for Neuroscience* **26**, 3120-3129 (2006). https://doi.org:10.1523/jneurosci.5392-05.2006

36 Qiang, L. *et al.* Tau does not stabilize axonal microtubules but rather enables them to have long labile domains. *Current Biology* **28**, 2181-2189. e2184 (2018).

37 Li, D. & Cho, Y. K. High specificity of widely used phospho-tau antibodies validated using a quantitative whole-cell based assay. *Journal of Neurochemistry* **152**, 122-135 (2020). https://doi.org:https://doi.org/10.1111/jnc.14830

38 Ercan, E. *et al.* A validated antibody panel for the characterization of tau post-translational modifications. *Molecular neurodegeneration* **12**, 1-19 (2017).

39 Ellis, M. J. *et al.* Validation of Tau antibodies for use in western blotting and immunohistochemistry. *BioRxiv*, 2023.2004. 2013.536711 (2023).

40 Mirbaha, H. *et al.* Seed-competent tau monomer initiates pathology in a tauopathy mouse model. *The Journal of biological chemistry* **298**, 102163 (2022). https://doi.org:10.1016/j.jbc.2022.102163

41 Lapasset, L. *et al.* Rejuvenating senescent and centenarian human cells by reprogramming through the pluripotent state. *Genes & development* **25**, 2248-2253 (2011).

42 Patterson, M. *et al.* Defining the nature of human pluripotent stem cell progeny. *Cell research* **22**, 178-193 (2012).

43 Capano, L. S. *et al.* Recapitulation of endogenous 4R tau expression and formation of insoluble tau in directly reprogrammed human neurons. *Cell Stem Cell* **29**, 918-932. e918 (2022).

44 Siahaan, V. *et al.* Kinetically distinct phases of tau on microtubules regulate kinesin motors and severing enzymes. *Nature Cell Biology* **21**, 1086-1092 (2019). https://doi.org:10.1038/s41556-019-0374-6

45 Zheng-Fischhöfer, Q. *et al.* Sequential phosphorylation of Tau by glycogen synthase kinase-3beta and protein kinase A at Thr212 and Ser214 generates the Alzheimer-specific epitope of antibody AT100 and requires a paired-helical-filament-like conformation. *Eur J Biochem* **252**, 542-552 (1998). https://doi.org:10.1046/j.1432-1327.1998.2520542.x

46 Goedert, M., Jakes, R. & Vanmechelen, E. Monoclonal antibody AT8 recognises tau protein phosphorylated at both serine 202 and threonine 205. *Neuroscience Letters* **189**, 167-170 (1995). https://doi.org:https://doi.org/10.1016/0304-3940(95)11484-E

47 Otvos, L., Jr. *et al.* Monoclonal antibody PHF-1 recognizes tau protein phosphorylated at serine residues 396 and 404. *J Neurosci Res* **39**, 669-673 (1994). https://doi.org:10.1002/jnr.490390607

48 Rye, D., Leverenz, J., Greenberg, S., Davies, P. & Saper, C. The distribution of Alz-50 immunoreactivity in the normal human brain. *Neuroscience* **56**, 109-127 (1993).

49 Dujardin, S. *et al.* Tau molecular diversity contributes to clinical heterogeneity in Alzheimer's disease. *Nature medicine* **26**, 1256-1263 (2020). https://doi.org:10.1038/s41591-020-0938-9

50 Mazet, F. *et al.* A high-density immunoblotting methodology for quantification of total protein levels and phosphorylation modifications. *Sci Rep* **5**, 16995 (2015). https://doi.org:10.1038/srep16995

51 Hanger, D. P., Betts, J. C., Loviny, T. L. F., Blackstock, W. P. & Anderton, B. H. New Phosphorylation Sites Identified in Hyperphosphorylated Tau (Paired Helical Filament-Tau) from Alzheimer's Disease Brain Using Nanoelectrospray Mass Spectrometry. *Journal of Neurochemistry* **71**, 2465-2476 (1998). https://doi.org:https://doi.org/10.1046/j.1471-4159.1998.71062465.x

52 Yang, Y. *et al.* Altered succinylation of mitochondrial proteins, APP and tau in Alzheimer's disease. *Nature Communications* **13**, 159 (2022). https://doi.org:10.1038/s41467-021-27572-2

53 Liu, F., Iqbal, K., Grundke-Iqbal, I., Hart, G. W. & Gong, C.-X. O-GlcNAcylation regulates phosphorylation of tau: A mechanism involved in Alzheimer's disease. *Proceedings of the National Academy of Sciences* **101**, 10804-10809 (2004). https://doi.org:doi:10.1073/pnas.0400348101

54 Ksiezak-Reding, H., Liu, W.-K. & Yen, S.-H. Phosphate analysis and dephosphorylation of modified tau associated with paired helical filaments. *Brain Research* **597**, 209-219 (1992). https://doi.org:https://doi.org/10.1016/0006-8993(92)91476-U

55 Köpke, E. *et al.* Microtubule-associated protein tau. Abnormal phosphorylation of a non-paired helical filament pool in Alzheimer disease. *Journal of Biological Chemistry* **268**, 24374-24384 (1993). https://doi.org:https://doi.org/10.1016/S0021-9258(20)80536-5

56 Biswas, S. *et al.* Tau accelerates tubulin exchange in the microtubule lattice. *Nature Physics* **21**, 1616-1628 (2025). https://doi.org:10.1038/s41567-025-03003-7

57 Fitzpatrick, A. W. P. *et al.* Cryo-EM structures of tau filaments from Alzheimer's disease. *Nature* **547**, 185-190 (2017). https://doi.org:10.1038/nature23002

58 Duan, P., Dregni, A. J., Mammeri, N. E. & Hong, M. Structure of the nonhelical filament of the Alzheimer's disease tau core. *Proceedings of the National Academy of Sciences* **120**, e2310067120 (2023). https://doi.org:doi:10.1073/pnas.2310067120

59 Zhao, W. *et al.* Cryo-EM structures reveal variant Tau amyloid fibrils between the rTg4510 mouse model and sporadic human tauopathies. *Cell Discovery* **10**, 27 (2024). https://doi.org:10.1038/s41421-023-00637-w

60 Falcon, B. *et al.* Structures of filaments from Pick's disease reveal a novel tau protein fold. *Nature* **561**, 137-140 (2018). https://doi.org:10.1038/s41586-018-0454-y

61 Yoshiyama, Y. *et al.* Synapse loss and microglial activation precede tangles in a P301S tauopathy mouse model. *Neuron* **53**, 337-351 (2007).

62 Naseri, N. N. *et al.* Aggregation of mutant cysteine string protein-alpha via Fe-S cluster binding is mitigated by iron chelators. *Nature structural & molecular biology* **27**, 192-201 (2020). https://doi.org:10.1038/s41594-020-0375-y

63 Santhosh Kumar, S. *et al.* Sequential CRISPR screening reveals partial NatB inhibition as a strategy to mitigate alpha-synuclein levels in human neurons. *Science Advances* **10**, eadj4767 (2024).

64 Xu, T. *et al.* The Proteoform Landscape of Tau from the Human Brain. *Journal of Proteome Research*, 2916-2925 (2025). https://doi.org:10.1021/acs.jproteome.5c00139

65 Kafader, J. O. *et al.* Multiplexed mass spectrometry of individual ions improves measurement of proteoforms and their complexes. *Nature Methods* **17**, 391-394 (2020). https://doi.org:10.1038/s41592-020-0764-5

66 Xie, Y. X. *et al.* Lysosomal exocytosis releases pathogenic α-synuclein species from neurons in synucleinopathy models. *Nature Communications* **13**, 4918 (2022).

67 Ramirez, J. *et al.* Multivalency drives interactions of alpha-synuclein fibrils with tau. *Plos one* **19**, e0309416 (2024).

68 Robinson, J. L. *et al.* Pathological combinations in neurodegenerative disease are heterogeneous and disease-associated. *Brain* **146**, 2557-2569 (2023). https://doi.org:10.1093/brain/awad059

69 Xu, H. *et al.* In vitro amplification of pathogenic tau conserves disease-specific bioactive characteristics. *Acta Neuropathologica* **141**, 193-215 (2021). https://doi.org:10.1007/s00401-020-02253-4

70 He, Z. *et al.* Amyloid-β plaques enhance Alzheimer's brain tau-seeded pathologies by facilitating neuritic plaque tau aggregation. *Nature medicine* **24**, 29-38 (2018). https://doi.org:10.1038/nm.4443

71 Lovestone, S., Hartley, C. L., Pearce, J. & Anderton, B. H. Phosphorylation of tau by glycogen synthase kinase-3β in intact mammalian cells: The effects on the organization and stability of microtubules. *Neuroscience* **73**, 1145-1157 (1996). https://doi.org:https://doi.org/10.1016/0306-4522(96)00126-1

72 Castoldi, M. & Popov, A. V. Purification of brain tubulin through two cycles of polymerization-depolymerization in a high-molarity buffer. *Protein Expr Purif* **32**, 83-88 (2003). https://doi.org:10.1016/s1046-5928(03)00218-3

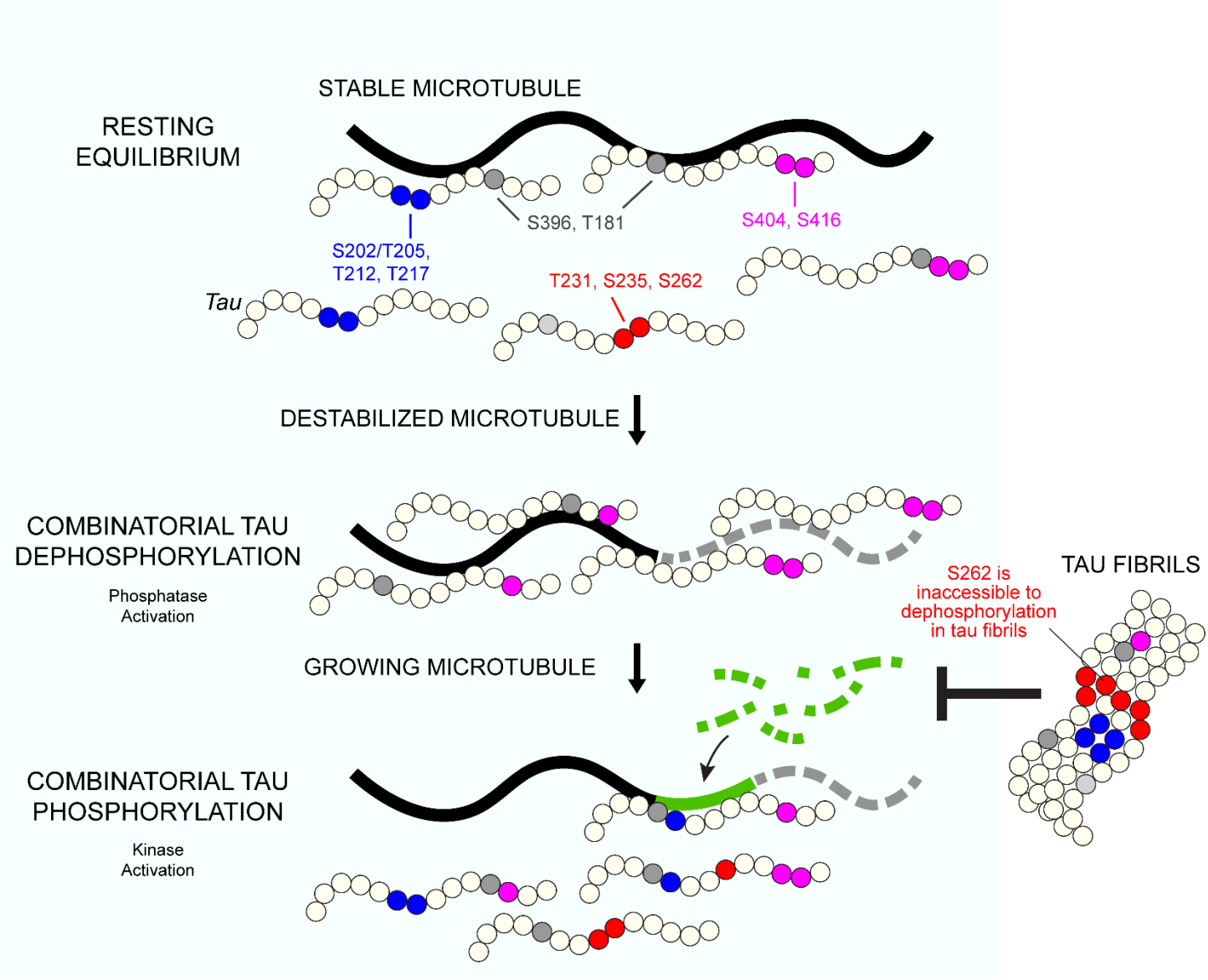

GRAPHICAL ABSTRACT

Schematic model of our findings: Tau phosphorylation is dynamically regulated in specific combinatorial patterns in response to shifting MT growth cycles.

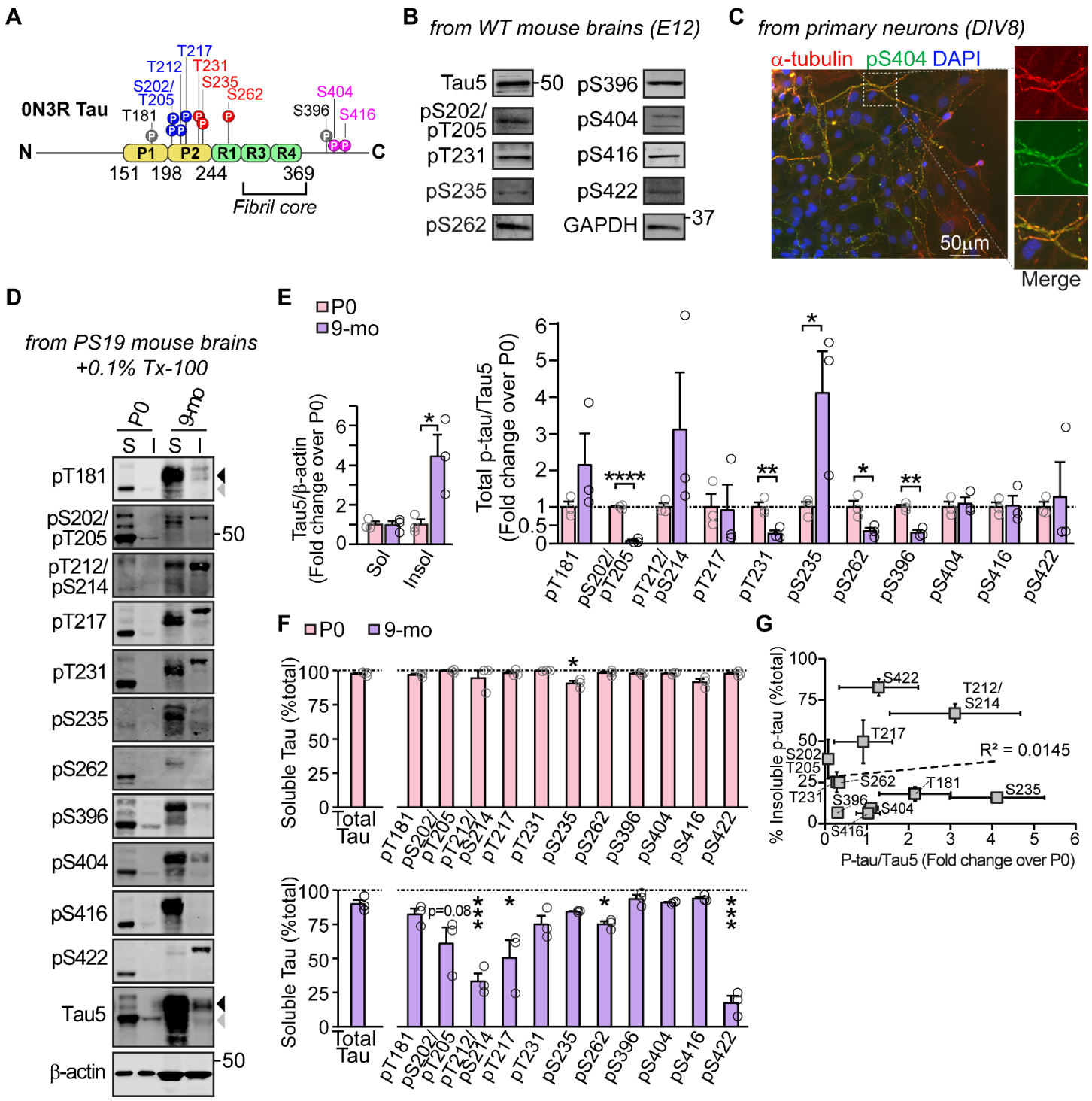

Figure 1- Tau phosphorylation levels in aged tauopathy mice do not correlate with its aggregation.

a) Schematic of the fetal human 0N3R tau isoform. Residue numbering is based on the 2N4R isoform, as is convention in the field. The phospho-epitopes that were probed in this study in iNeurons are indicated and consistently color-coded throughout. **b)** Brains were collected from wildtype mice on embryonic day 12 (E12). Following separation by SDS-PAGE, pan-tau (anti-Tau5) and p-tau sites were detected by immunoblot at the indicated epitopes. Immunoblots are representative of 6 embryonic mouse brains. **c)** Tau phosphorylated at S404 (green) colocalized with MT protein α-tubulin (red) in wildtype primary mouse neurons at *DIV*8. For **d-g**, PS19 mouse brains were collected at post-natal days 0 (P0) and at 9 months. N=3 littermates per time point. The band shift between P0 and 9 months represents 0N3R mouse tau (gray arrowhead) and 1N4R human tau (black arrowhead). **d)** Triton-X solubility from PS19 mouse brains was used to separate [S]oluble from

[I]nsoluble p-tau, followed by immunoblot. **e)** Pan-tau (anti-Tau5) solubility was quantified by Tau5/β-actin as a fold-change of P0 levels for both the soluble and insoluble fractions. Total p-tau levels (soluble + insoluble) were quantified and normalized to pan-tau (anti-Tau5) at each time point and represented as a fold-change of P0 levels. **f)** P-tau solubility was quantified as a percentage of total p-tau (soluble + insoluble) for each epitope and plotted alongside pan-tau solubility levels at each time point. Significance calculations were made compared to pan-tau solubility at each given age. **g)** The fold change in p-tau/Tau5 levels at 9-months compared to neonates (from 'Fig. 1e') was correlated with insoluble p-tau levels at 9-months of age (from 'Fig. 1f'). Immunoblots and quantifications are representative of n=3 littermates. All data are representative of mean ± SEM. *P<0.05; **P<0.01; ***P<0.001; ****P<0.0001 by Student's t-test.

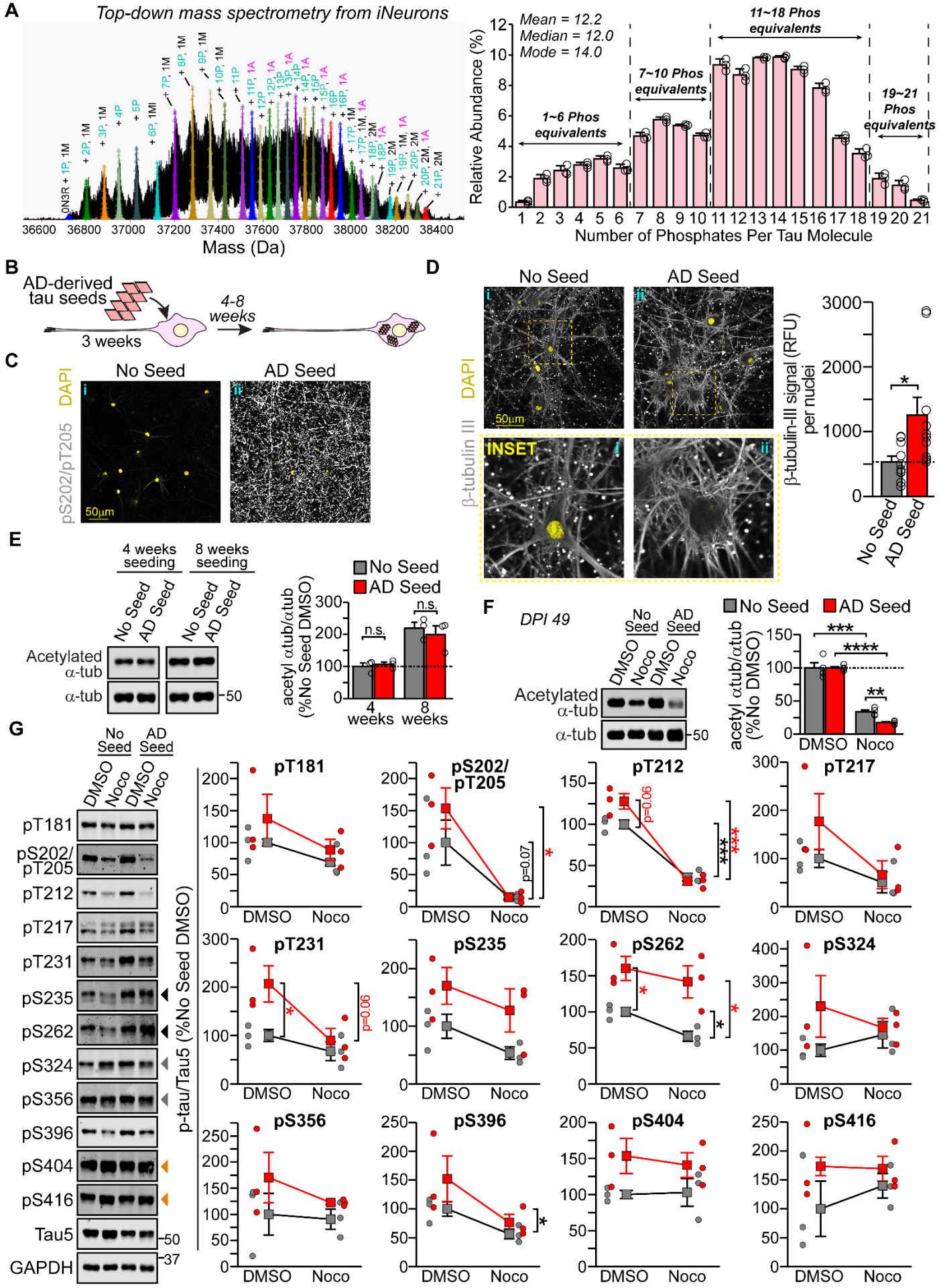
A
Top-down mass spectrometry from iNeurons
Mass (Da)
Mean = 12.2
Median = 12.0
Mode = 14.0
1~6 Phos equivalents
7~10 Phos equivalents
11~18 Phos equivalents
19~21 Phos equivalents
Relative Abundance (%)
Number of Phosphates Per Tau Molecule
B
AD-derived tau seeds
3 weeks
4-8 weeks
C
No Seed
AD Seed
DAPI
pS202/pT205
50µm
D
No Seed
AD Seed
DAPI
β-tubulin III
INSET
50µm
β-tubulin-III signal (RFU) per nuclei
E
4 weeks seeding
8 weeks seeding
No Seed
AD Seed
Acetylated α-tub
α-tub
acetyl αtub/αtub (%No Seed DMSO)
n.s.
4 weeks
8 weeks
F
DPI 49
DMSO
Noco
acetyl αtub/αtub (%No DMSO)
G
pT181
pS202/pT205
pT212
pT217
pT231
pS235
pS262
pS324
pS356
pS396
pS404
pS416
Tau5
GAPDH
p-tau/Tau5 (%No Seed DMSO)
p=0.07
p=0.06

171

Figure 2 – Tau aggregation disrupts the neuron's ability to counteract MT destabilization.

a) Tau was immunoprecipitated from iNeurons (*DPI 30*) with two pan-tau antibodies (Tau5 and HT7), and stoichiometries of phosphorylation events per tau protein were measured by top-down mass spectrometry with I^2MS technology, indicating up to 21 phosphates per tau protein. PTMs were assigned based on mass shifts of ~80 Da for phosphorylation, ~42 Da for acetylation and ~14 Da for methylation. The relative abundance of phosphate occupancy was calculated as a percentage of all detected 0N3R tau proteoforms. The annotated spectrum is representative of a single replicate of n=3 independent I^2MS injections. Quantifications represent mean ± STD for n=3 independent I^2MS injections. P = phosphorylation. A = acetylation. M = methylation. **b)** iNeurons were treated at 3 weeks post-differentiation with insoluble tau seeds derived from a post-mortem AD brain. Neurons were used for biochemistry or immunocytochemistry 4-8 weeks post-seeding. **For c-d**, soluble proteins were extracted from iNeurons by ice-cold methanol fixation at 6 weeks post-seeding (*DPI 63*). Images are representative of n=8 independent treatments. **c)** Immunocytochemistry was performed against anti-AT8 (pS202/pT205) at 40x magnification. Tau pathology was robust in neurons seeded with AD-derived tau. **d)** Immunocytochemistry was performed against anti-β-tubulin III at 60x magnification in neurons treated with either DMSO (control) or 10 μM nocodazole for 90 minutes. Quantification of β-tubulin III signal intensity from was performed using the mean signal intensity normalized to the number of nuclei in each field of view, from 10 random fields of view, for each sample group. **e)** Immunoblot and quantification of K40-acetylated α-tubulin normalized to α-tubulin 1A levels at 4-weeks (*DPI 49*) or 8-weeks (*DPI 77*) post-seeding. Blots and quantifications are representative of n=3 independent seeding and treatment experiments. For **f-g**, unseeded and seeded iNeurons were treated at 4 weeks post-seeding with either DMSO (control) or 10 μM nocodazole for 90 minutes, then harvested in RIPA buffer for Western blot. **f)** Immunoblot and quantification of K40-acetylated α-tubulin normalized to α-tubulin 1A levels. Blots and quantifications are representative of n=4 independent seeding and treatment experiments. **g)** Immunoblot against tau phosphorylated at the indicated phospho-epitopes. Blots and quantifications represent p-tau signal normalized to pan-tau for n=3 independent seeding and treatment experiments. The black arrowheads indicate the sites that responded uniquely to nocodazole treatment in seeded neurons. The gray arrowheads indicate sites that are contained with the tau fibril core. The orange arrowheads indicate two C-terminal sites that were differentially regulated in seeded versus unseeded neurons. All data are representative of mean ± SEM. *P<0.05; **P<0.01; ***P<0.001; ****P<0.0001 by Student's t-test. N.S. = not significant.

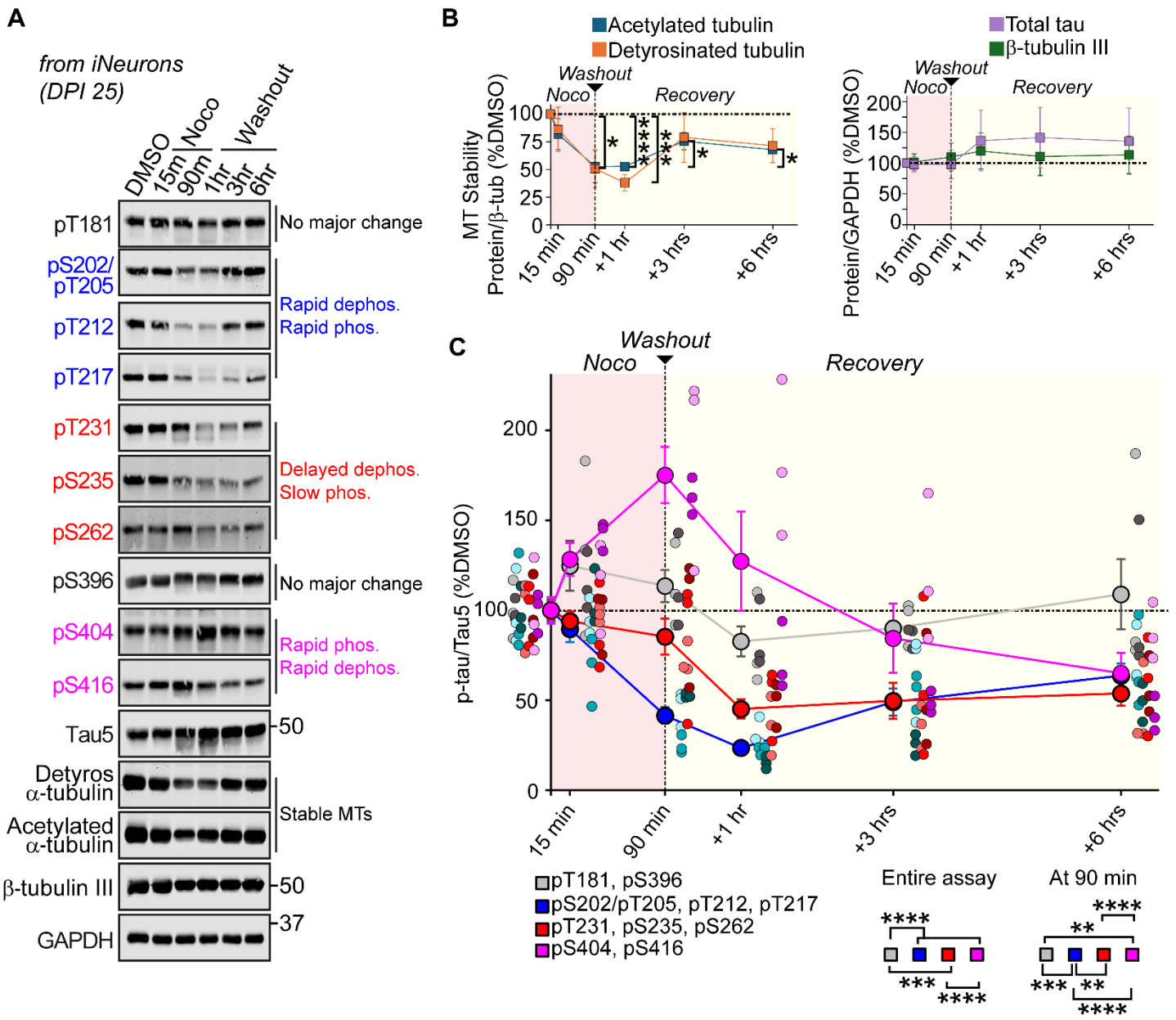

Figure 3: Phospho-sites throughout tau are differentially regulated to counteract MT destabilization.

iNeurons (*DPI 25*) were treated with either DMSO (control) or 10 μM nocodazole for either 15 min, 90 min, or 90 min followed by nocodazole washout and recovery for 1 hour, 3 hours or 6 hours. **a)** Samples were harvested for SDS-PAGE followed by immunoblot against the indicated proteins. N=3 independent cultures and treatments per group. **b)** Quantification of 'a' for MT stability as measured by changes to detyrosinated α-tubulin and K40 acetylated α-tubulin during nocodazole treatment and washout. Total (pan) tau and β-tubulin III levels were not significantly impacted throughout the assay. *P<0.05; ***P<0.001; ****P<0.0001 by Student's t-test. **c)** Quantification of 'a' for p-tau normalized to pan-tau. **P<0.01; ***P<0.001; ****P<0.0001 by post-hoc Tukey's HSD test.

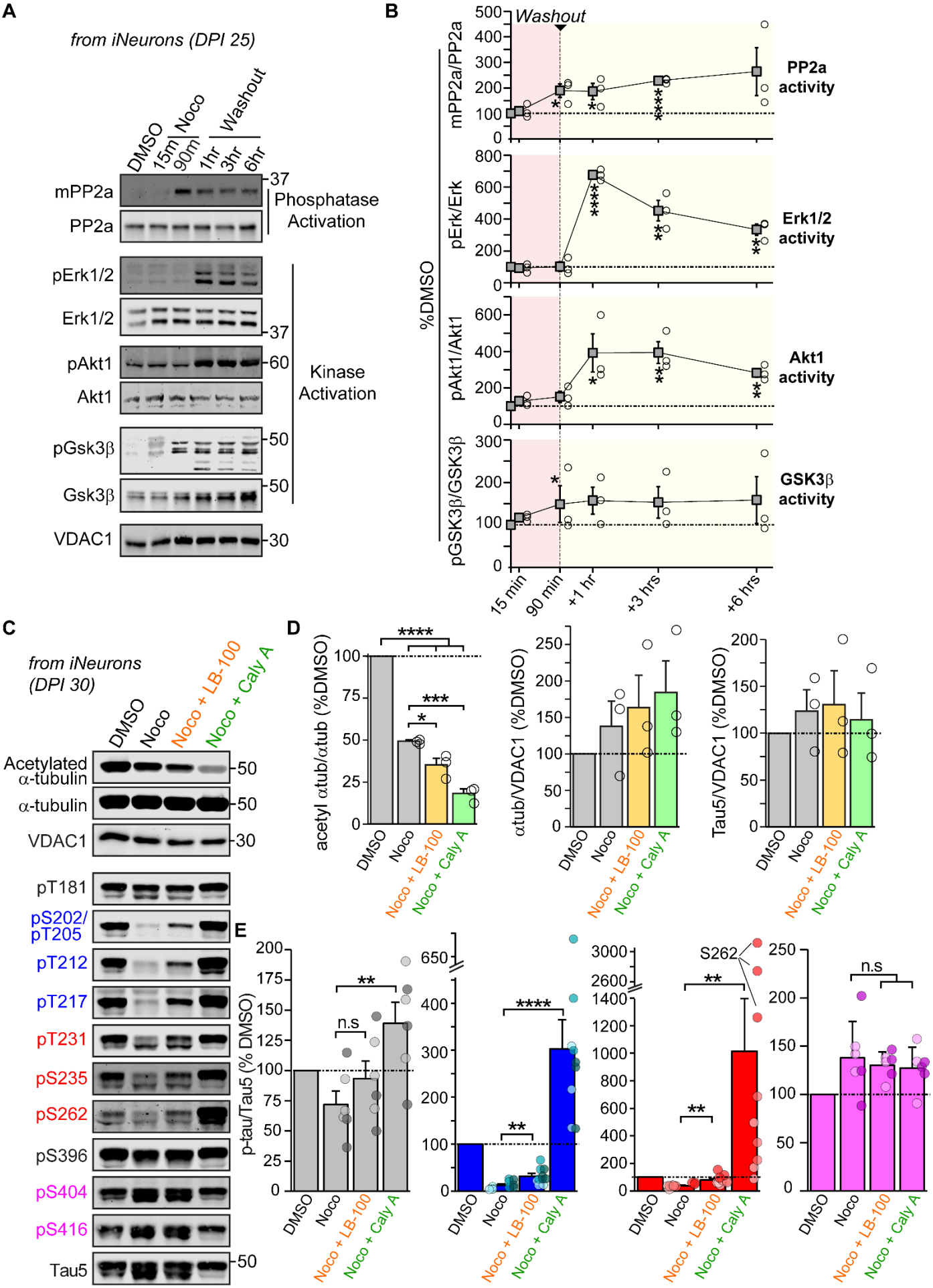
A
from iNeurons (DPI 25)
DMSO
Noco
Washout
15m
90m
1hr
3hr
6hr
mPP2a
PP2a
Phosphatase Activation
pErk1/2
Erk1/2
pAkt1
Akt1
pGsk3β
Gsk3β
Kinase Activation
VDAC1
37
60
50
30
B
Washout
%DMSO
mPP2a/PP2a
pErk/Erk
pAkt1/Akt1
pGSK3β/GSK3β
PP2a activity
Erk1/2 activity
Akt1 activity
GSK3β activity
15 min
90 min
+1 hr
+3 hrs
+6 hrs
C
from iNeurons (DPI 30)
DMSO
Noco
Noco + LB-100
Noco + Caly A
Acetylated α-tubulin
α-tubulin
VDAC1
pT181
pS202/pT205
pT212
pT217
pT231
pS235
pS262
pS396
pS404
pS416
Tau5
D
acetyl αtub/αtub (%DMSO)
αtub/VDAC1 (%DMSO)
Tau5/VDAC1 (%DMSO)
E
p-tau/Tau5 (% DMSO)
n.s
S262

219

220 **Figure 4 –Tau dephosphorylation by PP2a is necessary to counteract MT destabilization.**

221 **a)** iNeurons (*DPI 25*) were treated with either DMSO (control) or 10 μM nocodazole for either 15 min, 90 min, or 90 min
222 followed by nocodazole washout and recovery for 1 hour, 3 hours or 6 hours. PP2a activation was measured by methylation
223 at Leu309. Kinase activation was measured by phosphorylation against Erk1/2 (T202/T204), Akt1 (S473) and GSK3β
224 (Y216). **b)** Quantification of 'a'. Markers for kinase and phosphatase activation were normalized to their respective pan-
225 proteins: pErk1/2 (T202/T204) normalized to pan-Erk1/2, pAkt1 (S473) normalized to pan-Akt1, pGSK3β (Y216) normalized
226 to pan-GSK3β, and mPP2a (L309) normalized to pan-PP2a. Blots are representative of n=3 independent treatments.
227 Significance calculations were made compared to the initial timepoint. For **c-e**, iNeurons (*DPI 30*) were treated with either
228 DMSO (control), 10 μM nocodazole, or 10 μM nocodazole supplemented with either LB-100 (20 μM) or Calyculin A (20 nM)
229 for 90 min. N=3 independent cultures and treatments. **c)** Representative immunoblots are shown for the indicated proteins
230 and p-tau epitopes. **d)** Quantification of changes to MT stability by immunoblot against K40-acetylated α-tubulin normalized
231 to α-tubulin levels. No significant changes were detected to total α-tubulin or pan-tau (anti-Tau5) levels, normalized to
232 VDAC1. **e)** As in 'd', changes to p-tau were measured by immunoblot against the indicated phospho-epitopes. P-tau levels
233 were normalized to pan-tau (anti-Tau5) for each sample. N.S.=not significant. *P<0.05; **P<0.01; ***P<0.001; ****P<0.0001
234 by Student's t-test. All data are representative of mean ± SEM.

235

236

237

238

239

240

241

242

243

244

245

246

247

248

249

250

251

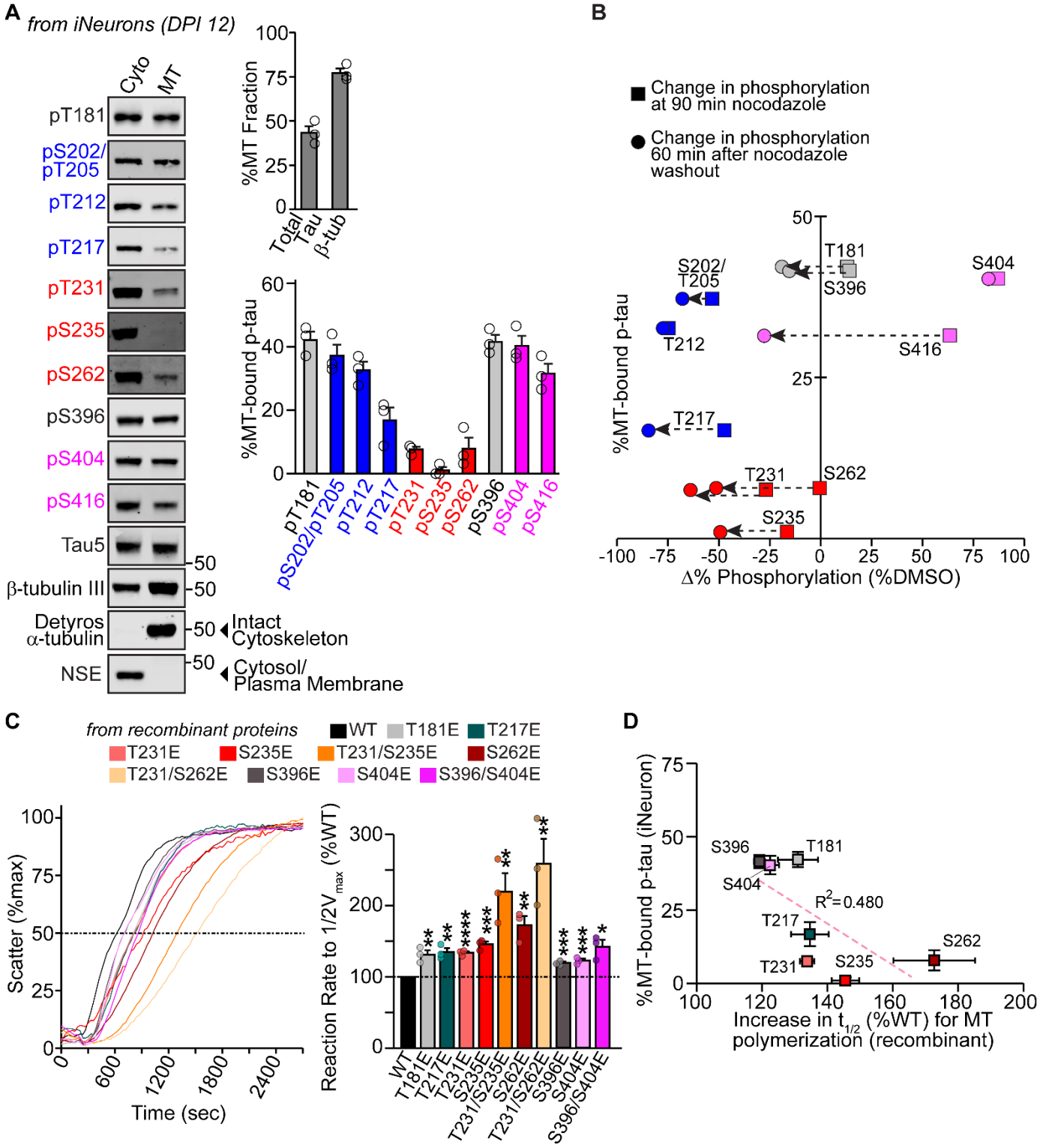

Figure 5: Site-specific phosphorylation directly disrupts tau's interaction with MTs.

a) MTs were fractionated from tau^{KD} iNeurons expressing 0N3R^{myc} at *DPI 12* (n=3 independent cultures, transductions and fractionations). SDS-PAGE followed by immunoblot was used to detect p-tau levels in cytosolic and MT-bound fractions. Separation of detyrosinated α-tubulin (MT fraction, only) from neuron-specific enolase (NSE), a cytosol-specific protein (cytosolic fraction, only), indicated successful separation of intact MTs from the cytosol. The amounts of pan-tau (anti-Tau5), β-tubulin III and p-tau that were found in the MT-bound fraction were quantified as a percentage of total protein (cytosolic + MT fractions) for each indicated target. **b)** The percentage of each p-tau epitope bound to MTs (from 'Fig. 5A') was plotted

260 alongside the changes in phosphorylation relative to DMSO treatment at 90 minutes of nocodazole treatment and 1 hour
261 after washout (from 'Fig. 3D'), revealing the trends in dephosphorylation over time. **c)** MT polymerization was detected *in*
262 *vitro* by light scatter at 340 nm for recombinant wildtype tau or phospho-mimics of each at the indicated sites. The reaction
263 mixture (20 μM soluble tubulin + 10 μM recombinant tau in BRB80 buffer) was supplemented with 1 mM DTT (final), initiated
264 by addition of 1 mM GTP (final) at 37C and monitored for 45 minutes on a spectrophotometer. N=3 independent
265 polymerization reactions for each tau variant. Quantification of the change in the reaction rate to 50% V_{max} for each phospho-
266 mimic was compared to wildtype tau. **d)** The percentage of MT-bound p-tau from iNeurons (from 'Fig. 5a') was plotted
267 alongside the increase in $t_{1/2}$ rate of MT polymerization by tau phospho-mimics compared to WT (from 'Fig. 5c'), for epitopes
268 T181, T217, T231, S235, S262, S396 and S404. All data are representative of mean ± SEM. *P<0.05; **P<0.01; ***P<0.001;
269 ****P<0.0001 by Student's t-test.

270

271

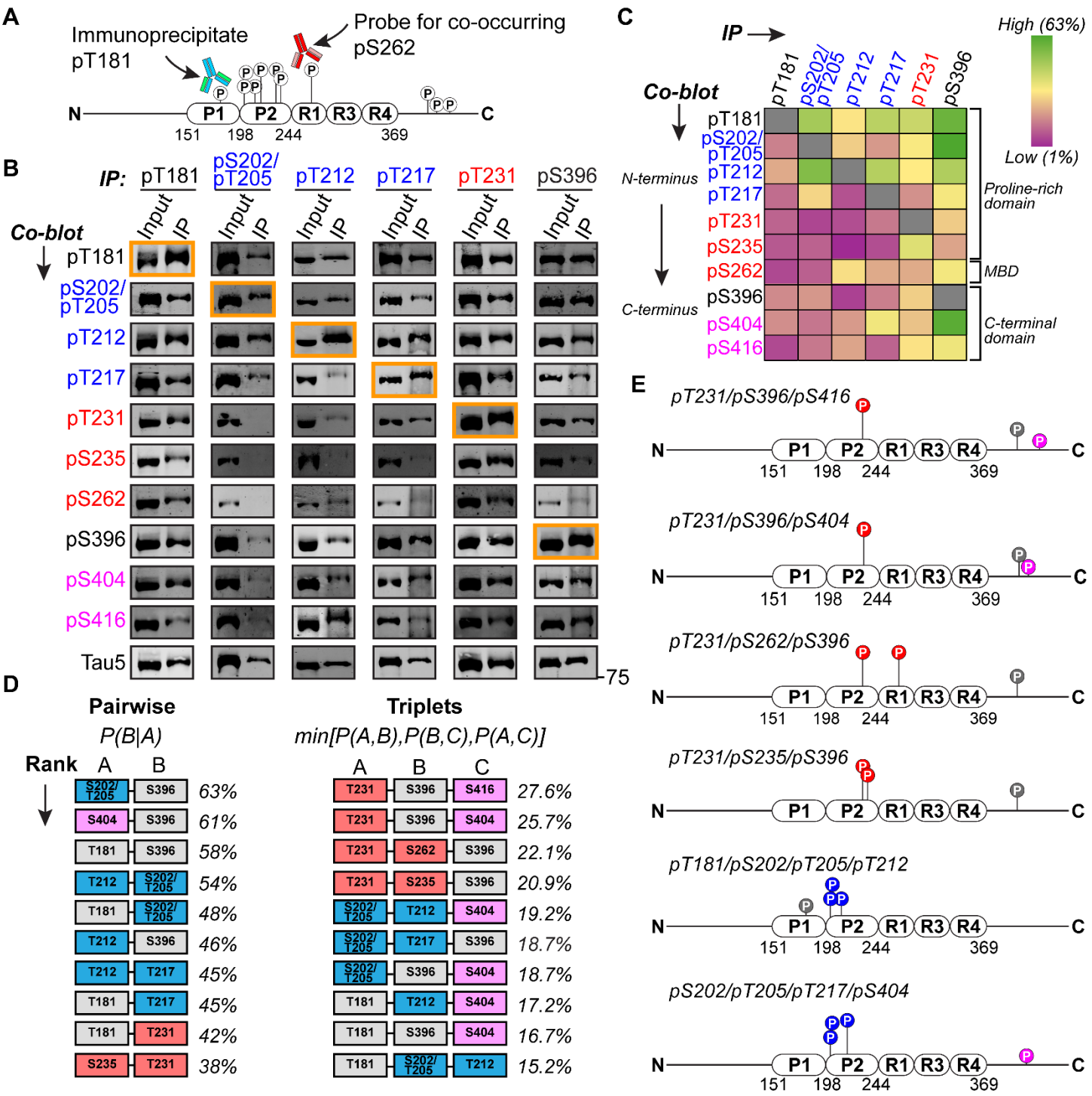

Figure 6: Phospho-epitopes are co-phosphorylated in specific patterns in iNeurons.

a) General workflow for p-tau immunoprecipitation from iNeurons under denaturing conditions, followed by blotting for co-occurring phospho-epitopes. **b)** Tau^{KD} iNeurons were lentivirally transduced with 0N3R^{EGFP}. P-tau was immunoprecipitated at 32 days post-induction, followed by separation by SDS-PAGE and immunoblotted against the indicated immunoprecipitated p-tau epitope and co-blotted at various p-tau epitopes. The immunoblot outlined in orange indicates the immunoprecipitated p-tau species in that given column of immunoblots. Blots are representative of n=4 (pT181, pT212, pS396), n=5 (pS202/pT205) and n=6 (pT217, pT231) independent cultures and immunoprecipitations. **c)** Heat map representing the quantification of phospho-site co-occurrence for each immunoprecipitated p-tau species, as described in the 'Methods' section. Green=high co-occurrence. Purple=low co-occurrence. Data is representative of n=4 (pT181, pT212,

282 pS396), n=5 (pS202/pT205) and n=6 (pT217, pT231) independent cultures and immunoprecipitations. **d)** The top 10 most
283 common combinations of two and three co-occurring phospho-epitopes are ranked from top to bottom. For pairwise
284 combinations, the percentages adjacent to each combination reflect the highest linkage for a given pair of phospho-epitopes.
285 Combinations of three phospho-epitopes were predicted by minimum linkage analysis as described in the 'Methods' section.
286 The percentages adjacent to each triplet represent the lowest co-occurrence probability between any of the three indicated
287 epitopes. **e)** Schematic representation of several predicted combinatorial phospho-modifications to 0N3R tau in iNeurons.

288

289

290

291

292

293

294

295

296

297

298

299

300

301

302

303

304

305

306

307

308

309

310

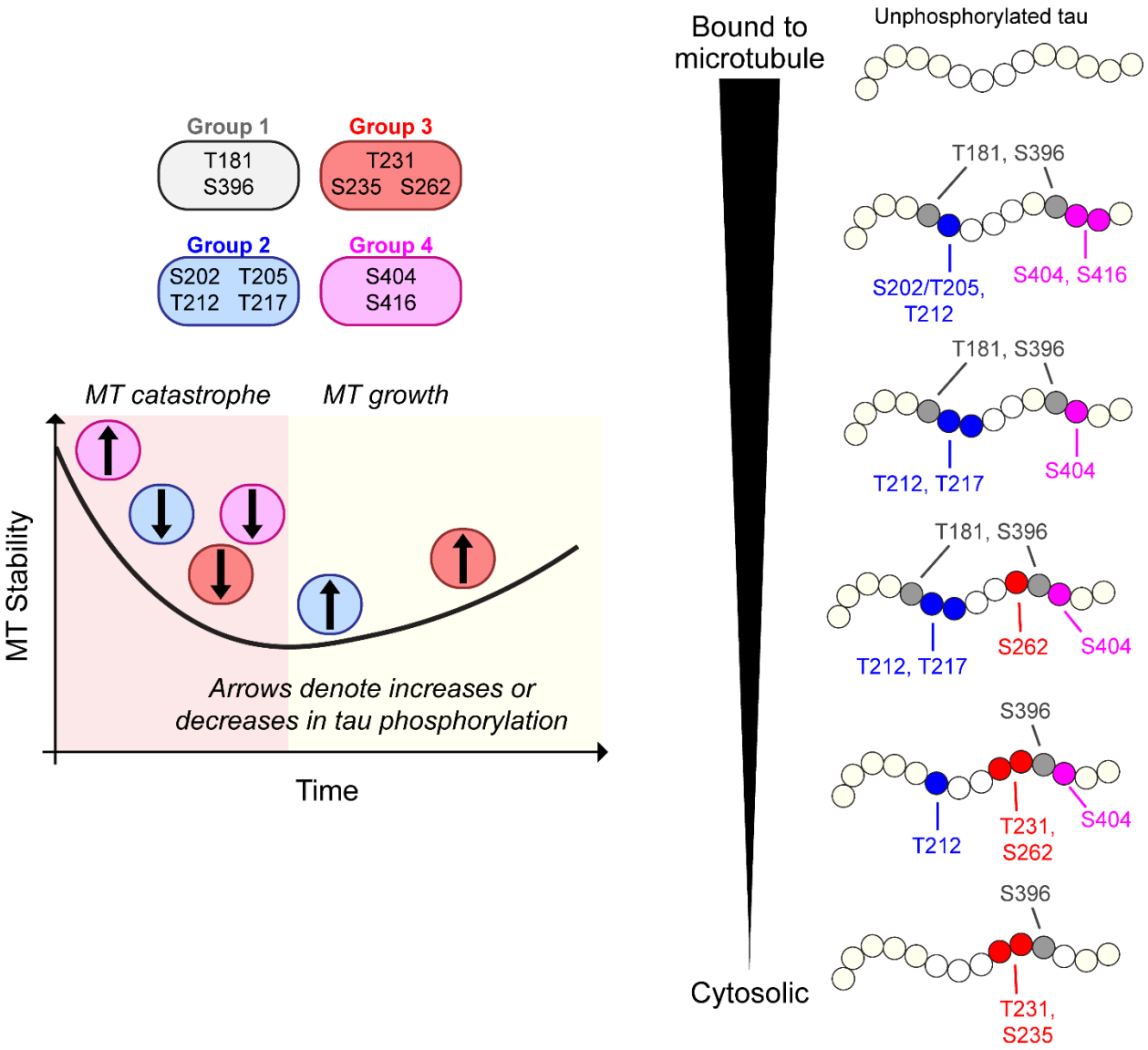

Figure 7: Schematic summary

Temporal changes to site-specific phosphorylated occur in specific combinations in response to MT collapse and growth. Based on co-occurrence linkage of phospho-epitopes, fractionation of MT-bound and cytosolic proteins, and changes to site-specific phosphorylated during MT collapse and recovery, we present predictions of the likelihood that certain combinatorial phospho-modifications to tau are found bound to or dissociated from MTs.